Meteorol Atmos Phys 82, 139–170 (2003)
DOI 10.1007/s00703-001-0595-6

Meteorology and Atmospheric Physics
Printed in Austria

[1] Center for Analysis and Prediction of Storms, University of Oklahoma, Norman, OK 73019, USA
[2] School of Meteorology, University of Oklahoma, Norman, OK 73019, USA

The Advanced Regional Prediction System (ARPS), storm-scale numerical weather prediction and data assimilation

Ming Xue[1,2], **Donghai Wang**[1,*], **Jidong Gao**[1], **Keith Brewster**[1], and **Kelvin K. Droegemeier**[1,2]

With 12 Figures

Received May 7, 2001; revised October 15, 2001
Published online: November 21, 2002

Summary

In this paper, we first describe the current status of the Advanced Regional Prediction System of the Center for Analysis and Prediction of Storms at the University of Oklahoma. A brief outline of future plans is also given. Two rather successful cases of explicit prediction of tornadic thunderstorms are then presented. In the first case, a series of supercell storms that produced a historical number of tornadoes was successfully predicted more than 8 hours in advance, to within tens of kilometers in space with initiation timing errors of less than 2 hours. The general behavior and evolution of the predicted thunderstorms agree very well with radar observations. In the second case, reflectivity and radial velocity observations from Doppler radars were assimilated into the model at 15-minute intervals. The ensuing forecast, covering a period of several hours, accurately reproduced the intensification and evolution of a tornadic supercell that in reality spawned two tornadoes over a major metropolitan area. These results make us optimistic that a model system such as the ARPS will be able to deterministically predict future severe convective events with significant lead time. The paper also includes a brief description of a new 3DVAR system developed in the ARPS framework. The goal is to combine several steps of Doppler radar retrieval with the analysis of other data types into a single 3-D variational framework and later to incorporate the ARPS adjoint to establish a true 4DVAR data assimilation system that is suitable for directly assimilating a wide variety of observations for flows ranging from synoptic down to the small nonhydrostatic scales.

* Current address: NASA Langley Research Center, Hampton, VA 23681-2199.

1. Introduction

In 1989, the Center for Analysis and Prediction of Storms (CAPS) was established at the University of Oklahoma as one of the National Science Foundation's first 11 Science and Technology (S&T) Centers. Its formal mission was to *demonstrate the practicability of storm-scale numerical weather prediction and to develop*, *test*, *and validate a regional forecast system appropriate for operational*, *commercial*, *and research applications*. Its ultimate vision was to make available a fully functioning storm-scale NWP system (Lilly, 1990; Droegemeier, 1990).

To achieve the above mission, an advanced prediction model system was needed. It was decided that this model had to meet a number of criteria. First, it had to be able to assimilate, through modern data assimilation strategies, new data of higher temporal and spatial density (e.g., those from the WSR-88D Doppler radar network) than had traditionally been available.

Second, the model had to serve as an effective tool for studying the dynamics and predictability of storm-scale weather in both idealized and realistic numerical weather prediction (NWP) settings. It must also handle atmospheric phenomena ranging from regional scales down to micro-scales as interactions across this spectrum are known to have profoundly important impacts on storm-scale phenomena. The model also had to be able to run efficiently on modern parallel computing platforms. These needs required that the model have a flexible and general dynamic and computational framework and include comprehensive physical processes.

Despite the availability of a number of nonhydrostatic research models at the time of its establishment, CAPS chose to develop an entirely new model for a number of reasons. First, most existing models were initially developed by individuals for specific research problems and they have since undergone considerable modifications and thus reflect the disparate programming styles of each contributor. Some of these models evolved from their hydrostatic predecessors started decades ago. Such codes are often poorly documented and therefore require substantial efforts to learn and are even harder to modify for the rapid investigation of scientific ideas. Second, such model codes were developed mostly on older generation computers and in many cases require substantial re-tooling for modern, especially distributed-memory, parallel processors. Third, the assimilation of observational data on the thunderstorm scale is particularly challenging, especially with four-dimensional variational method based on the adjoint technique (Kapitza, 1991; Sun et al, 1991). The creation of the adjoint code is a tedious process prone to error and can be greatly simplified by a careful design of the forward model. Further, care in developing the forward model can also greatly facilitate the use of automated tools for obtaining the adjoint (Talagrand, 1991; Bischof et al, 1992). Finally, a well-designed model framework will also facilitate the implementation of more accurate numerical techniques and model physics.

For the above reasons, an entirely new, three-dimensional, nonhydrostatic model *system* known as the Advanced Regional Prediction System (ARPS) was developed. It is a comprehensive multi-scale prediction system that includes data ingest, quality control, and objective analysis packages, single-Doppler radar parameter retrieval and data assimilation procedures, the prediction model, as well as post-processing packages and validation tools (Fig. 1). By the end of its predetermined 11-year life as a NSF S&T center, we believe that CAPS has largely accomplished its original ambitious goals. Currently, CAPS continues as a center under the support of a number of initiatives and grants.

The numerical prediction component of the ARPS is a three-dimensional, nonhydrostatic

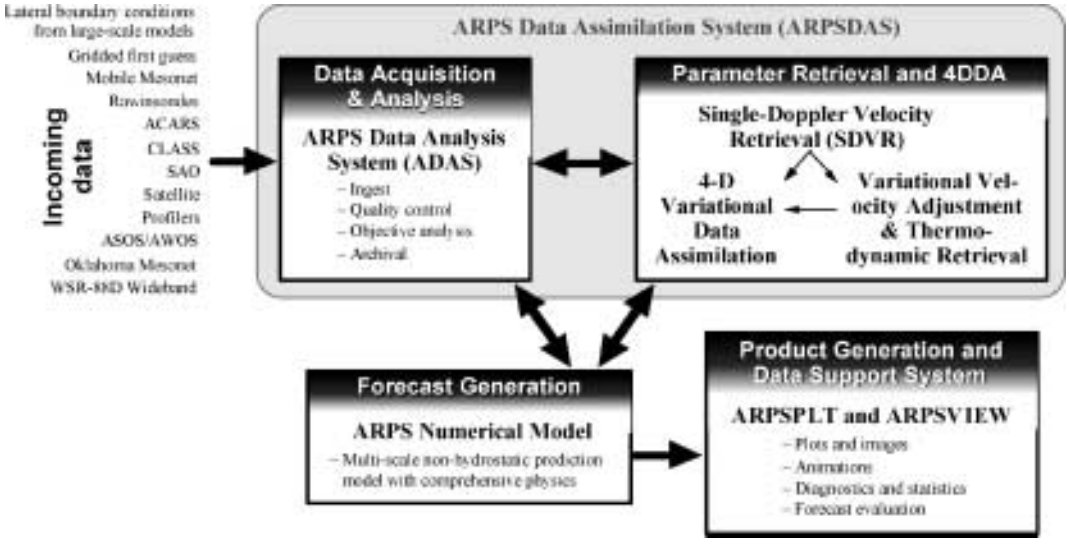

Fig. 1. The principal components of the ARPS system

compressible model formulated in generalized terrain-following coordinates. It is designed from the beginning to run on computing platforms ranging from single-processor scalar workstations to massively parallel scalar or vector processors. Guided by modern software engineering theories and practices, the entire system is written in a consistent style and is easy to use, extend and maintain. The code is also extensively documented and the system has served as an effective research, educational and prediction tool for a variety of applications by users throughout the world. The ARPS contains a comprehensive physics package and a self-contained data analysis, radar data retrieval and assimilation system. It has been subjecting to real-time weather prediction testing over several regions since mid-90s (e.g., Droegemeier et al, 1996; Xue et al, 1996a; Droegemeier, 1997; Carpenter et al, 1999; Shin et al, 1998). In the spring 1998, ARPS participated in a unique multi-model mesoscale ensemble prediction experiment organized by the CAPS, and the results are summarized in Hou et al (2001).

The ARPS, that existed in the form of a typical cloud model, was first made available to the public in 1992 (CAPS, 1992). The first comprehensive description of the formulation, numerical solution methods, physics parameterizations, computational implementation and configuration instructions for the system is given in the ARPS Version 4.0 User's Guide (Xue et al, 1995). More recent improvements and model verifications are described in Xue et al (2000; 2001). In this paper, we describe in Sect. 2 the current capabilities of the ARPS. Two sets of predictions at thunderstorm-resolving resolutions are presented in Sects. 3 and 4. The first case starts from the analysis of conventional data and predicts the initiation and evolution of a series of tornadic thunderstorms. In the second case, a rapid update assimilation cycle, including the analysis of cloud fields using Doppler radar data, is employed and the model successfully predicts the development and evolution of pre-existing thunderstorms. Section 5 describes the recently developed ARPS 3DVAR system and discusses certain issues of data assimilations at the small nonhydrostatic scales, in particular those related to the use of radar data. Section 5 also presents an example analysis using the 3DVAR system and its comparison with the analysis using ARPS Data Analysis System (ADAS). Section 6 concludes with an overall summary of the paper.

2. Current features of the ARPS system

ARPS version 4.0 was officially released in mid-1995. Since then, many improvements have been made to the system and many sub-releases were made available on the CAPS anonymous FTP server (ftp://ftp.caps.ou.edu/ARPS). In late 2000, the entire system was converted to Fortran 90 free-format using an automatic code converter customized to conform the ARPS Fortran 90 coding standard. Dynamic memory allocation was subsequently implemented manually for all programs. Significant development and improvements with the ARPS system since the Version 4 release include:

- A completely new real-time data ingest and analysis system (ADAS, Brewster, 1996) capable of handling a variety of data sources, including raw and retrieved Doppler radar and satellite data;
- A cloud analysis component in the ADAS that creates three-dimensional fields of cloud water, rainwater and improved fields of water vapor and temperature (Zhang et al, 1998; Zhang and Carr, 1998; Zhang, 1999);
- An integrated package for single-Doppler velocity and thermodynamic retrievals together with the associated variational adjustment procedures (Shapiro et al, 1995a; 1995b; 1996; Weygandt et al, 1998);
- A long and short-wave radiation package based on that of the NASA Goddard Space Flight Center (Chou, 1990; 1992; Chou and Suarez, 1994);
- The Skamarock adaptive grid refinement that supports multiple level two-way interactive grid nesting and run-time addition, removal and movement of nested grids (Skamarock and Klemp, 1993; Xue et al, 1993);
- Kain–Fritsch (Kain and Fritsch, 1993) cumulus parameterization;
- A non-local PBL parameterization based on 1.5-order TKE turbulence scheme (Xue et al, 1996b);
- A sophisticated three-phase ice microphysics (Lin et al, 1983; Tao et al, 1989), along with

the Schultz (1995) simplified ice microphysics, in addition to the previously available Kessler warm-rain scheme;
- Inclusion of snow cover and refinement of the land surface-vegetation model;
- High resolution (as fine as 100 m) terrain, land-use and land-cover data bases and the option to define multiple soil types in each grid cell to take advantage of the high-resolution soil-type data base;
- An ensemble prediction component using the scaled lagged averaged forecasting (SLAF) technique for generating initial and boundary condition perturbations (Ebisuszki and Kalnay, 1991; Hou et al, 2001);
- A flux-corrected transport (FCT) monotonic scalar advection option plus an efficient positive-definite advection scheme based on leap-frog-centered scheme (Zalesak, 1979; Lafore, 1998; Xue et al, 2000) in addition to the quadratically conserving second- and fourth-order advection (Xue and Lin, 2001);
- Options for monotonic high-order numerical diffusion (Xue, 2000);
- A radiation top-boundary condition with a relaxed limitation at the top lateral boundaries (Xue et al, 2000);
- Map factor in dynamic equations and provision for stretching in horizontal as well as the vertical directions (Xue et al, 2000);
- The use of the full density, instead of base-state density, in the pressure gradient force terms and the elimination of approximations in early versions of the dynamic equations;
- Support for gridded data sets from various operational models (e.g., RUC, ETA and AVN), the NCAR-NCEP global reanalysis as well as ARPS's own forecast to provide the analysis background and boundary conditions;
- Streamlined support for distributed memory platforms (e.g., the Cray T3E, SGI Origin; IBM SP, and NEC SX series, and workstation clusters including Linux PCs) via a message passing interface (MPI);
- Significant code optimization, including that achieved by removing differencing operators and by using lookup tables for expensive mathematical functions;
- A soil model initialization procedure using antecedent precipitation index (API, see e.g., example of use in Xue et al, 1998) or NCEP model fields, and an option to perform precycling of the soil model to obtain a balanced initial condition;
- A sophisticated Perl-based automated procedure for real-time data ingest, analysis and prediction control and web posting;
- Significantly enhanced graphics post-analysis programs;
- Support of several additional data formats (e.g., Vis5D, GRIB, GrADS, HDF, NetCDF) and their associated display and visualization tools;
- Several new Doppler radar analysis and retrieval schemes (Gao et al, 1999; 2001b; 2001c; Shapiro et al, 1999) and the associated pre-processing programs;
- A phase-correction scheme for adjusting the model or model-background states for phase or position errors in the forecast based on radar and other observations (Brewster, 1999; Brewster, 2002a; 2002b);
- A version of 4DDA scheme based on the full-model adjoint (Wang et al, 1995; 1997; Gao et al, 1998);
- A version of three-dimensional variational data assimilation system (3DVAR, Gao et al, 2001a).

A fully tested, Fortran 90 version was released in 2002 as ARPS version 5.0. The primary focus for the next few years at CAPS will be the continued development of the three-dimensional variational (3DVAR) system that will incorporate radar data retrievals and the analysis of all other data types in one single unified variational framework. The 3DVAR system will be a natural successor to the current ADAS and will serve as the foundation for a complete 4DVAR system based on the full model adjoint. We will also continue to improve the model physics, including those for precipitation and land surface processes. We will calibrate and improve the current and future versions of the land surface model in the ARPS using direct soil temperature and moisture measurements from the Oklahoma Mesonet, and design and test a soil state variable retrieval system based on the soil model and its adjoint. In addition, we will implement a new two-way nesting capability that will run on distributed memory parallel platforms. Information on all aspects of the ARPS system can be found at

http://www.caps.ou.edu/ARPS. In the following two sections, we will present results from the ARPS as applied to explicit prediction of thunderstorm-scale weather. Before moving on to the next sections, we point out that the unique features in small-scale data assimilation, especially of Doppler radar data, careful computational design and parallel implementation of the model system from the beginning (Droegemeier et al, 1995; Johnson et al, 1994), and the choice of the state-of-the-science numerical techniques and physics parameterizations made the model uniquely suitable for our mission, namely, storm-scale research and NWP.

3. ARPS prediction of the January 21–23, 1999 Arkansas tornado outbreak case

3.1. Case introduction

A major tornado outbreak occurred during the afternoon and evening of January 21, 1999 in the state of Arkansas (AR), in the central U.S. Fifty-six tornadoes were reported statewide with the strongest tornadoes rated F3 (maximum winds 71 ms^{-1} to 92 ms^{-1}) on the Fujita scale. Most of the tornadoes occurred between 4 and 11 pm CST, or between 22 UTC January 21 and 05 UTC January 22. Eight people were killed by the tornadoes. It is believed to be the largest tornado outbreak in Arkansas. The number of tornadoes in this single event is nearly triple the historical average number of 21 per year in the state. The fact that this event occurred in January makes it even more unusual. In fact, this case had the most tornadoes ever in a single state for the month of January.

This event occurred during the extended period of CAPS AMS-99 (1999 American Meteorological Society Annual Meetings) real-time forecasting experiment, when CAPS was running the model on triple nested grids with the finest grid at 3-km grid spacing. Further study of this case has been made after the event, using larger domains for all three grids and higher resolutions for the intermediate (6-km) and finest (2-km) grids, and extending the forecast to 48 hours. Furthermore, intermittent data assimilation cycles are performed at the coarsest-resolution (32-km) grid. The goal is to examine the model's ability to forecast the entire sequence of events down to the convective-storm scales, including storms with strong rotating characteristics during the period of the tornado outbreak, and later the organization of storms leading to a long-lived propagating squall line. The results should also give insight into the predictability of events on the convective-storm scales. Furthermore, a successful prediction of the sequence of events offers us a valuable data set that can be further analyzed for understanding the dynamic and physical processes involved. Sensitivity experiments can be performed to further our understanding.

The synoptic-scale features and events of this case have been documented in Xue (2001), together with the prediction results on the 32-km and 6-km grid. In summary, the tornado outbreak occurred ahead of a deepening upper-level trough whose trough line was located over western Texas (TX). The upper-level wind backed slightly from west–southwesterly to southwesterly 12 UTC through 00 UTC. At the surface, a low that was over the Rockies earlier descended to the lee (east) side and expanded in size. The center remained in southwestern Oklahoma (OK) for this 12-hour period. At 00 UTC, January 22, a surface cold front was found extending from the surface low center to southwest (SW) TX, while a quasi-stationary front extended from the low center northeastward then eastward through Missouri (MO) all the way to the east coast of the United States. The area of tornado outbreak was therefore located in warm sector of the surface low, several hundreds of km ahead of the surface cold front. South of a SW–NE diagonal line bisecting Arkansas, the low-level flow was southerly for the entire 12-hour period and the observed CAPE reached 2000 J/kg south of this line. During the several hours surrounding 00 UTC January 22, most of the supercell storms that spawn tornadoes moved northeastwards along this diagonal line. In the 36 hours following the tornado outbreak, subsequent convection organized into an intense long-lasting squall line that moved east across much of eastern US, and finally into the Atlantic Ocean.

3.2. ARPS model forecast

The ARPS forecasts on the 32- and 6-km grids starting from 12 UTC January 21 and valid at 00 UTC January 22 and at 12 UTC January 23 were

presented in Xue et al (2001), along with a brief discussion on the results. At the end of that period, a squall line that matched very well with observations was obtained that extended north–south across the entire east coast of the US. In this paper, we focus on the results of the nested 2-km grid, for the period spanning the tornado outbreak. Particular attention is paid to the timing, location and characteristics of the model predicted storms, as compared to radar observations.

All runs started from 12 UTC, January 21, 1999. A 24-h long hourly intermittent data assimilation cycle was performed on the 32-km grid to achieve the best reproduction of the synoptic scale state of the atmosphere. The 6-km grid started from the 12 UTC ADAS analysis and was forced by the 32-km solutions at the lateral boundaries. All available observations, including data from the Oklahoma Mesonet data and the central-plains wind profiler demonstration network were used. The 2-km grid was initialized from interpolated 6-km analysis, without further addition of data. Because the initial time precedes the times with significant convective storms in the primary area of interest, no radar data (at least those in precipitation mode) were available for use in the initial analysis. It is therefore up to the model to initiate the convective storms several hours after the model initial time. Additional details on the model configuration can be found in Xue et al (2001).

As an overview, we first present in Fig. 2 a comparison of the simulated composite radar reflectivity field from the 32-km model with the observed one. It can be seen in the portion of domain having radar observations, the model

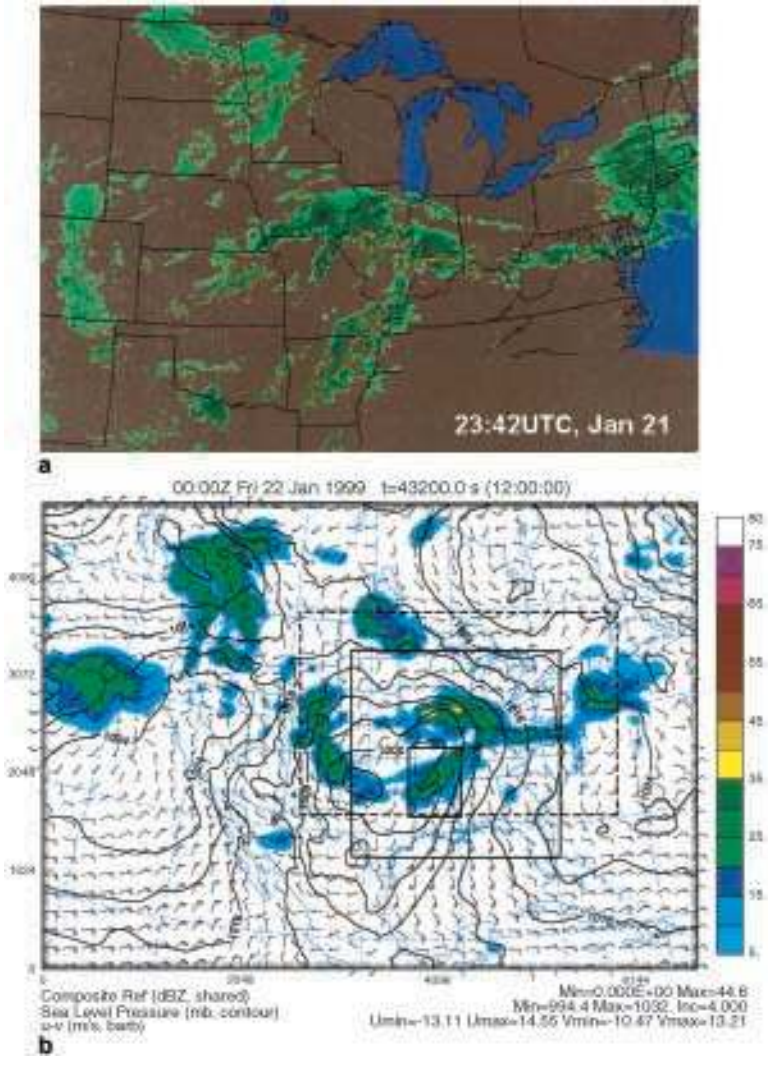

Fig. 2. Observed radar composite reflectivity field (**a**), and ARPS (**b**) surface winds, mean sea-level pressure (contours) and composite reflectivity field (shaded contours) at 00 UTC January 22, 1999 on the 32-km grid, corresponding to 12 h model time. The domain in (**a**) corresponds to the thick dashed box in (**b**). The two solid boxes in (**b**) indicate the 6- and 2-km domains

reflectivity pattern matches very well with the observed one. This includes an elongated precipitation region across the SW–NE axis of AR and the generally east–west oriented precipitation bands associated with a quasi-stationary front to the north. The areas of light precipitation over the Rockies, eastern North Dakota into western Minnesota, and over New Jersey and the surrounding region are also well reproduced. However, the model, at 32 km resolution, is not capable of producing high reflectivity values comparable to the observed ones in Arkansas, where tornadic thunderstorms were at their full strength at this time. It should be noted that the Kain–Fritsch cumulus parameterization option was used together with the explicit ice microphysics scheme on this grid. The reflectivity field presented does not include the parameterized convective precipitation. The field of total precipitation rate (not shown), however, does match the reflectivity pattern closely at this time, with the most noticeable difference being at the southern end of diagonal reflectivity region where additional parameterized precipitation was found. Cumulus parameterization was not used on either the 6- or 2-km grid.

3.3. Comparisons of 2-km resolution model forecasts with radar observations

To examine the detailed development and evolution of explicitly resolved storms as well as their timing and locations, we present in Fig. 3 side-by-side comparisons of model and observed reflectivity fields at 1 to 2 hour intervals. The model reflectivity field is calculated from model hydrometeors including rain water, snow and hail, according to the following semi-empirical formula adapted from Rogers and Yau (1989):

$$Z = 10\log_{10}\{17300(1000\rho q_r)^{7/4} + 38000[1000(q_s + q_h)]^{11/5}\},$$

where q_r, q_s and q_h are mixing ratios of rain water, snow and hail, respectively. SI units are used in the formula, with Z in dBZ. Snow and hail are not differentiated in this particular formula, obviously not a very good assumption. To make composite reflectivity images, the maximum value in a column is displayed. Furthermore, considering the semi-empirical nature of the formula, the model reflectivity fields should be compared with the observed ones in a semi-quantitative sense only.

From the observed reflectivity fields in Fig. 3, we see that convective cells first developed near the southwest corner of Arkansas. Shortly before 20 UTC, January 21, i.e., 2 pm local standard time (LST), three discrete cells can already be seen, with the maximum reflectivity values being less than 55 dBZ. At this time, these cells are still at their developing stage. At the same time, much of the 2-km model domain is filled with low values of reflectivity, in a way that is very similar to the 32- and 6-km grids (see Fig. 4 and Fig. 5). The maximum reflectivity is between 30 and 35 dBZ. Despite the lack of isolated intense convection in the model, the regions of highest reflectivity matches the observed areas of high reflectivity, including the regions of thunderstorm activities in SW Arkansas. The east–west oriented high reflectivity region about one third of the domain from the northern boundary is due to the lifting on the southern slope of the Ozark Plateau, which includes the Boston Mountains with peak height of about 580 meters on the model grid. The descent on the north side of the Plateau is responsible for the reflectivity minimum to the north. The upslope enhancement of reflectivity is also evident in the observed radar data.

In the model, reflectivity values greater than 40 dBZ started to appear shortly after 20 UTC. At 21 UTC (Fig. 3d), a series of cells in an E–W oriented line is found along the northern edge of the high reflectivity region, previously-noted to be due to orographic lifting. In the radar observation, apart from one significant cell, the reflectivity pattern corresponding to these cells is much weaker, though still apparent. The three cells in SW AR found at 20 UTC have fully developed by this time, and appear to have gone through cell splitting at least once (Fig. 3c). The cells move northeastward at about $20\,\mathrm{ms}^{-1}$. The convective activity in the model in the SW portion of AR is much weaker. Only one major cell is found, located about one county (~ 20 km) too far to the northwest (Fig. 3d) relative to the real cells (Fig. 3c).

By 22 UTC, the leading storm cell in the SW–NE oriented line had advanced to NE Faulkner county (Fig. 3e), the county north of Little Rock, located at the center of the plotted domain

(marked by letter L in Fig. 3a). It spawned the first two F2 tornadoes and caused 6 injuries in one of the homes according to the National Weather Service's storm data. Outside this line, a few weaker isolated storms formed to the east. In the model, most intense storms are found near the northern state boundary, a result of the northward propagation of the line found near the northern boundary at 21 UTC (Fig. 3f). Clearly these storms were over-predicted by the model.

Corresponding to the actual intense storms, which extended from the domain center to the SW corner, are model storms that are still at their formative stages in SW–NE lines, about 1 to 2 counties to the northwest. The individual cells in the model moved northeastward, in agreement with the observed storm motion (Fig. 3f). Major development occurred in the model in the 15-minute period between 2200–2215 UTC, with several new cells appearing near the SW corner of the domain, close to the southern state boundary while those cells seen at 22 UTC near the SW corner of Arkansas began to intensify. By 22:30 UTC, a series of cells organized in a SSW–NNE oriented line were already exhibiting hook-shaped echoes indicating significant updraft rotation (not shown). By 23 UTC, both the storms originating in the southwest and those to the north have become fully developed (Fig. 3h). Their reflectivity fields all exhibit a strong reflectivity gradient on their southwest flanks with many exhibiting hook-like appendages while the surface wind fields show strong convergence into the storms.

The first F3 tornado was reported at around 22:30 UTC in Dallas County, located in the south-central part of the domain (indicated by letter D in Fig. 3g), where a relatively isolated storm is clearly depicted. In the next half an hour, three more F3 tornadoes were reported in White, Independence and Monroe counties (indicated by letters W, I and M respectively in Fig. 3g), each corresponding to a major storm found in Fig. 3g. Many more weaker tornadoes were also reported. The model solution showed a marked increase in the low level vorticity after 22 UTC (not shown) which matched, or slightly lagged in the time, this first wave of intense tornado activity.

At 23 UTC, about a dozen storm cells can be identified both in radar observations and in the model, and both model and real storms exhibit isolated supercell storm characteristics with rotation more readily identifiable in the model. Zoomed-in plots of observed reflectivity fields also show hook-echo shapes and strong reflectivity gradients in some of the cells.

For the next three hours, from 23 UTC to 02 UTC January 22, both observation and model showed new cells being continually generated at the south end of the convective line while older cells moved along the diagonal axis across the state. In the model, while the cells moved in the correct directions, the line orientation is rotated a bit toward a north–south orientation relative to the observations, a result of the cell origination points being a couple of counties too far to the east and the convection to the north being initially displaced to the west. By the end of this three-hour period, the line in the model has turned more into the SW–NE orientation. As more cells were created through splitting process and the low-level cold pool spread, the storms in both the model and the real world became closer to each other and some, especially the older ones in the northern part, started to join together, creating connected line segments. At 02 UTC, the southern end of the observed and modeled lines were still touching the south–southwest state corner of Arkansas (Fig. 3k and Fig. 3l).

In the two hours following 02 UTC, the trend for the cells to merge and form a continuous line continued both in the model and in the real world (Fig. 3m and Fig. 3n). New cells stopped forming after 02 UTC (8 pm local time) as the boundary layer cooled after sunset, decreasing CAPE and increasing convective inhibition (CIN). By 04 UTC, the southern end of the primary line is two-to-three counties away from the southern

Fig. 3. Observed (left panel) and predicted (right panel) composite (column maximum) reflectivity fields from 20 UTC January 21 through 06 UTC January 22, 1999. The observed fields are from Little Rock, Arkansas WRS-88D radar and the predicted ones from the ARPS 2-km forecast. The plotting area is about 220 km on each side. The state and county boundaries are plotted at thick and thin lines, respectively. Little Rock is located at the center of domain, marked by letter L in (**a**). The typical counties are about 20 to 25 km across

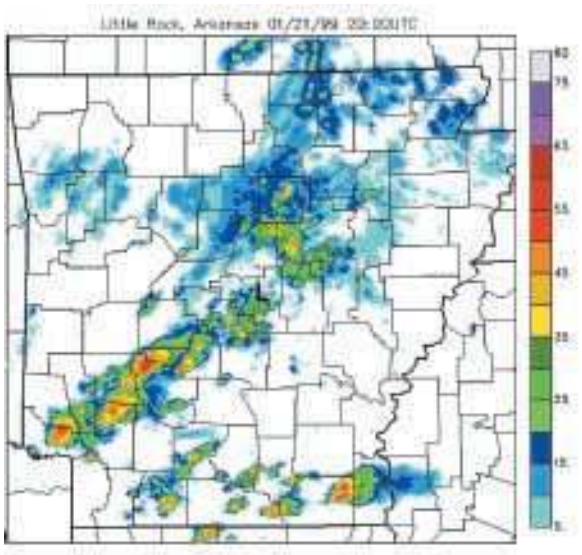
Little Rock, Arkansas 01/21/99 20:00UTC

a

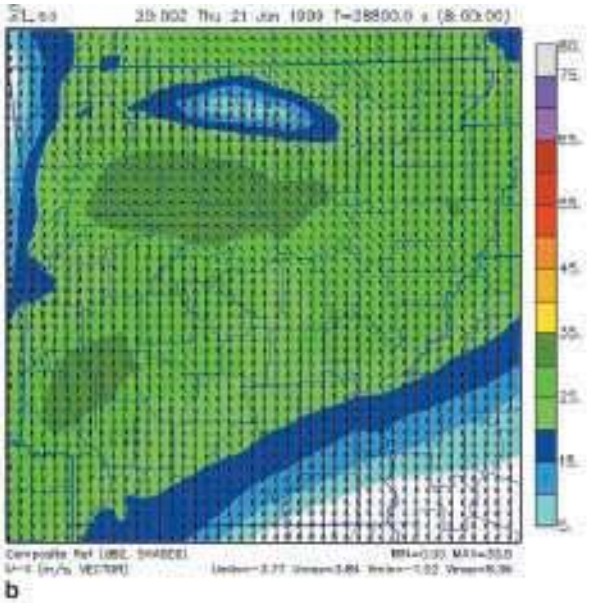
20:00Z Thu 21 Jan 1999 T=28800.0 s (8:00:00)

b

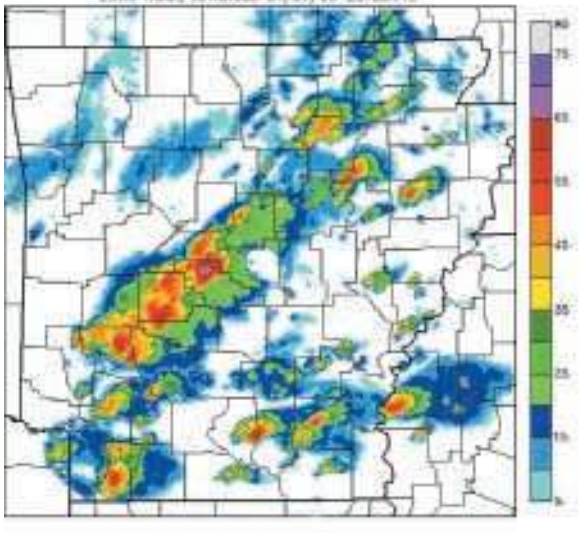
Little Rock, Arkansas 01/21/99 20:58UTC

c

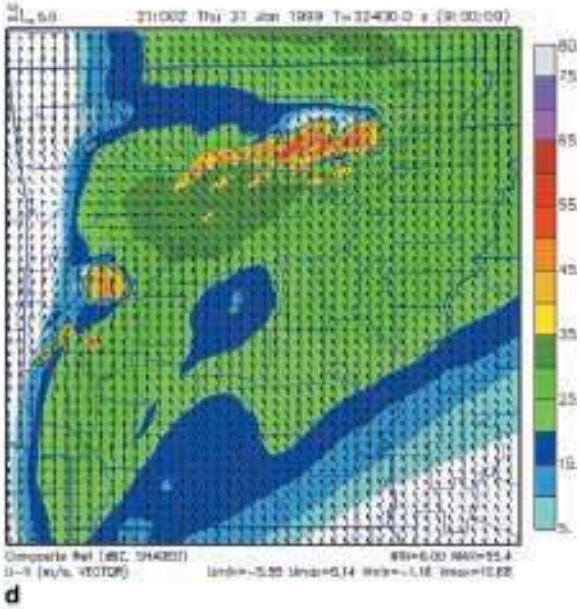
21:00Z Thu 21 Jan 1999 T=32400.0 s (9:00:00)

d

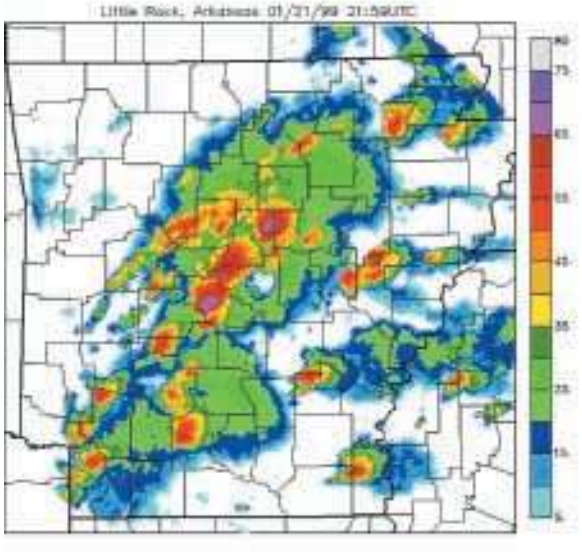
Little Rock, Arkansas 01/21/99 21:58UTC

e

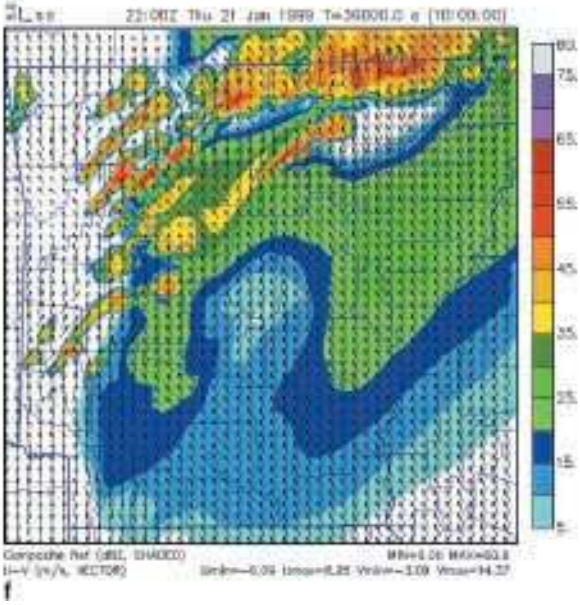
22:00Z Thu 21 Jan 1999 T=36000.0 s (10:00:00)

f

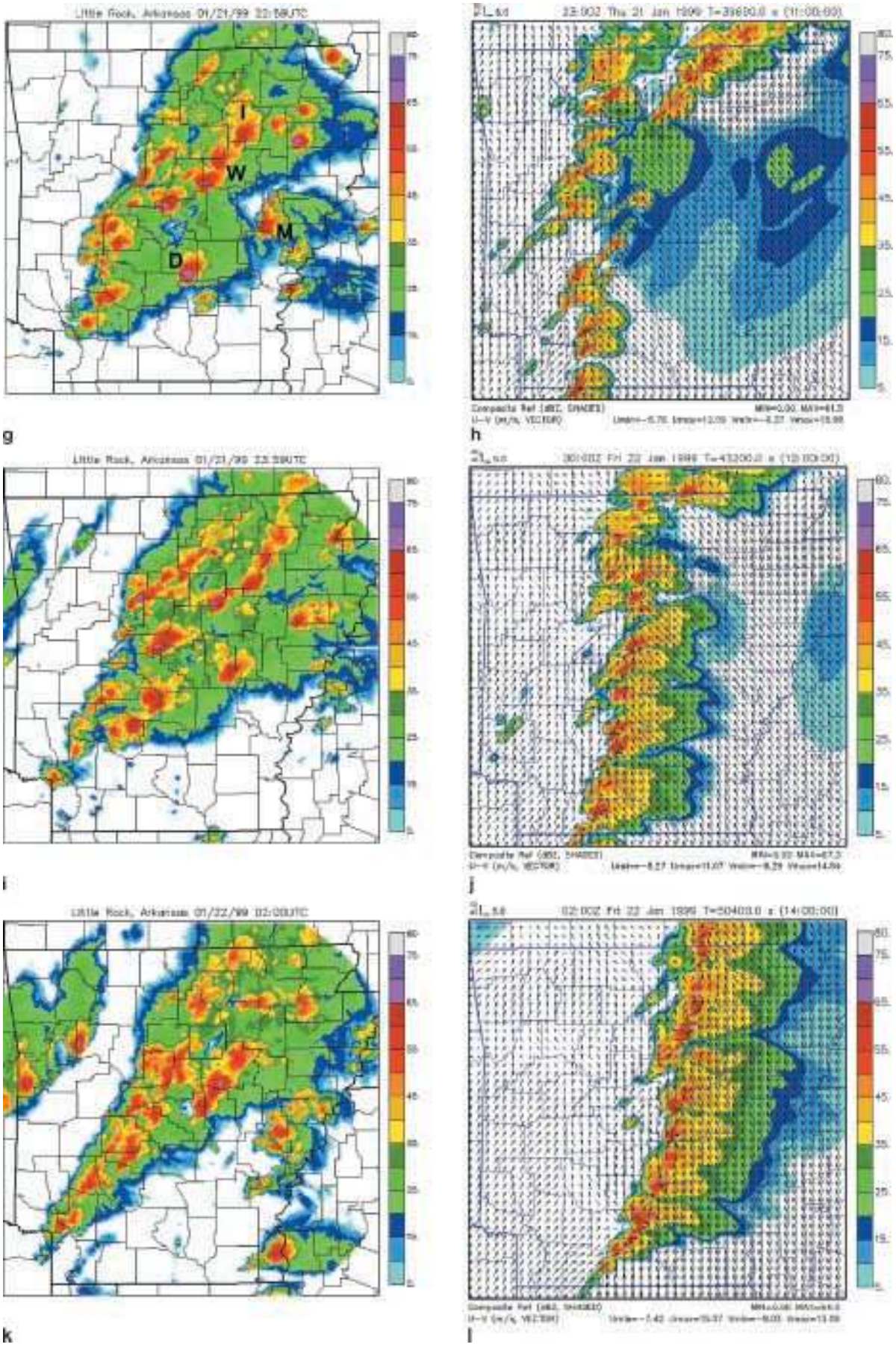

Fig. 3 (*continued*)

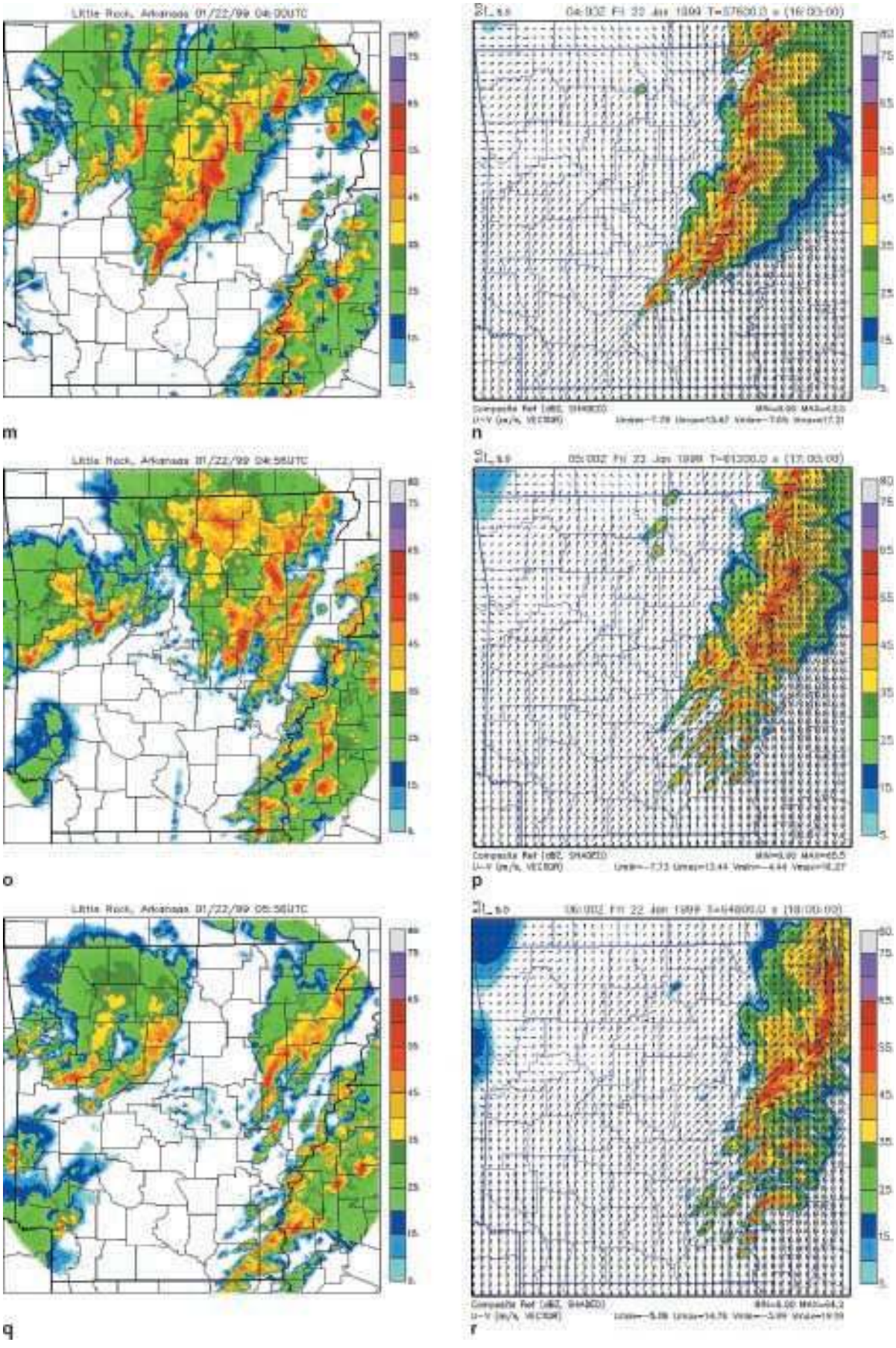

Fig. 3 (*continued*)

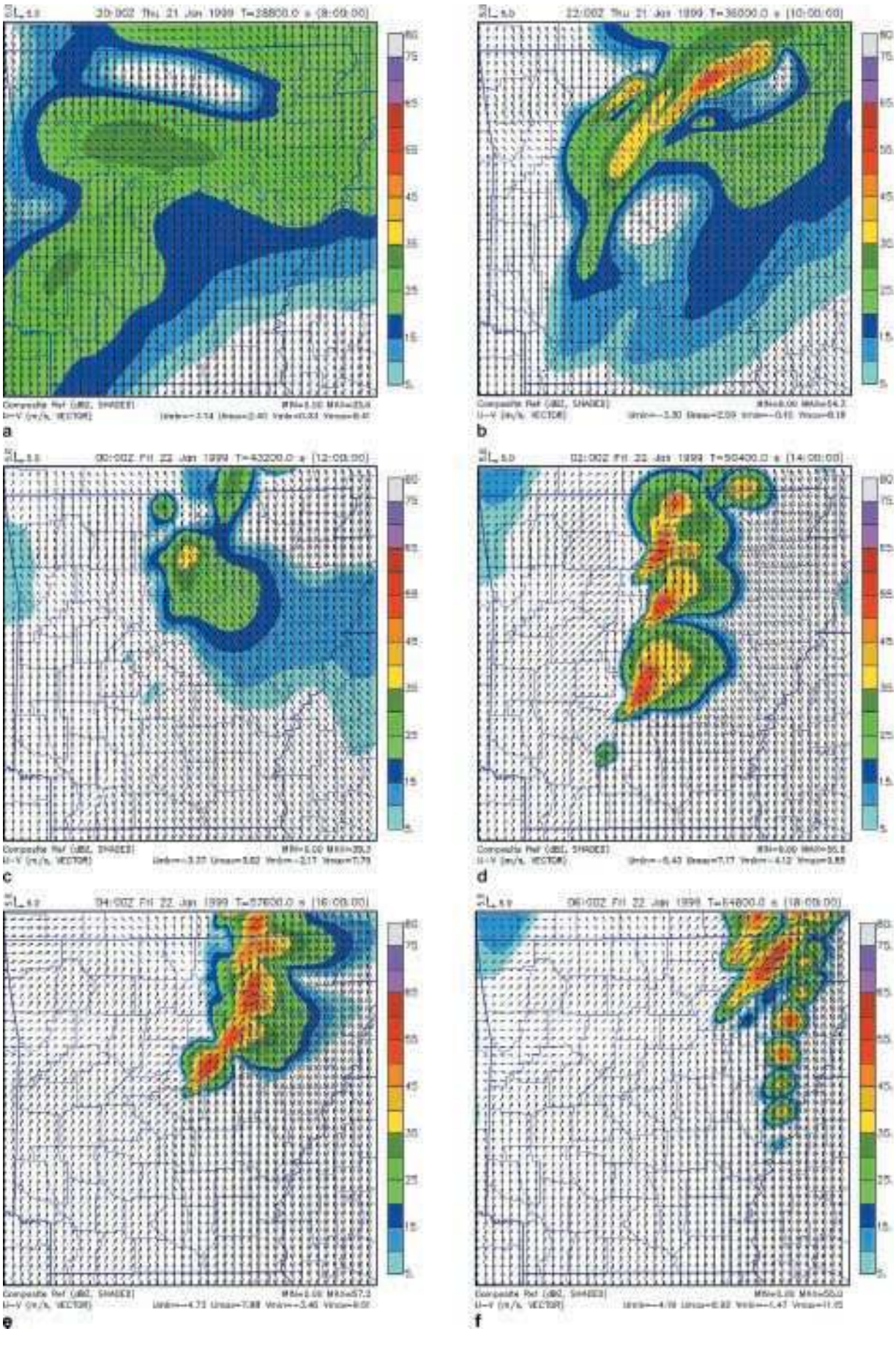
a
b
c
d
e
f

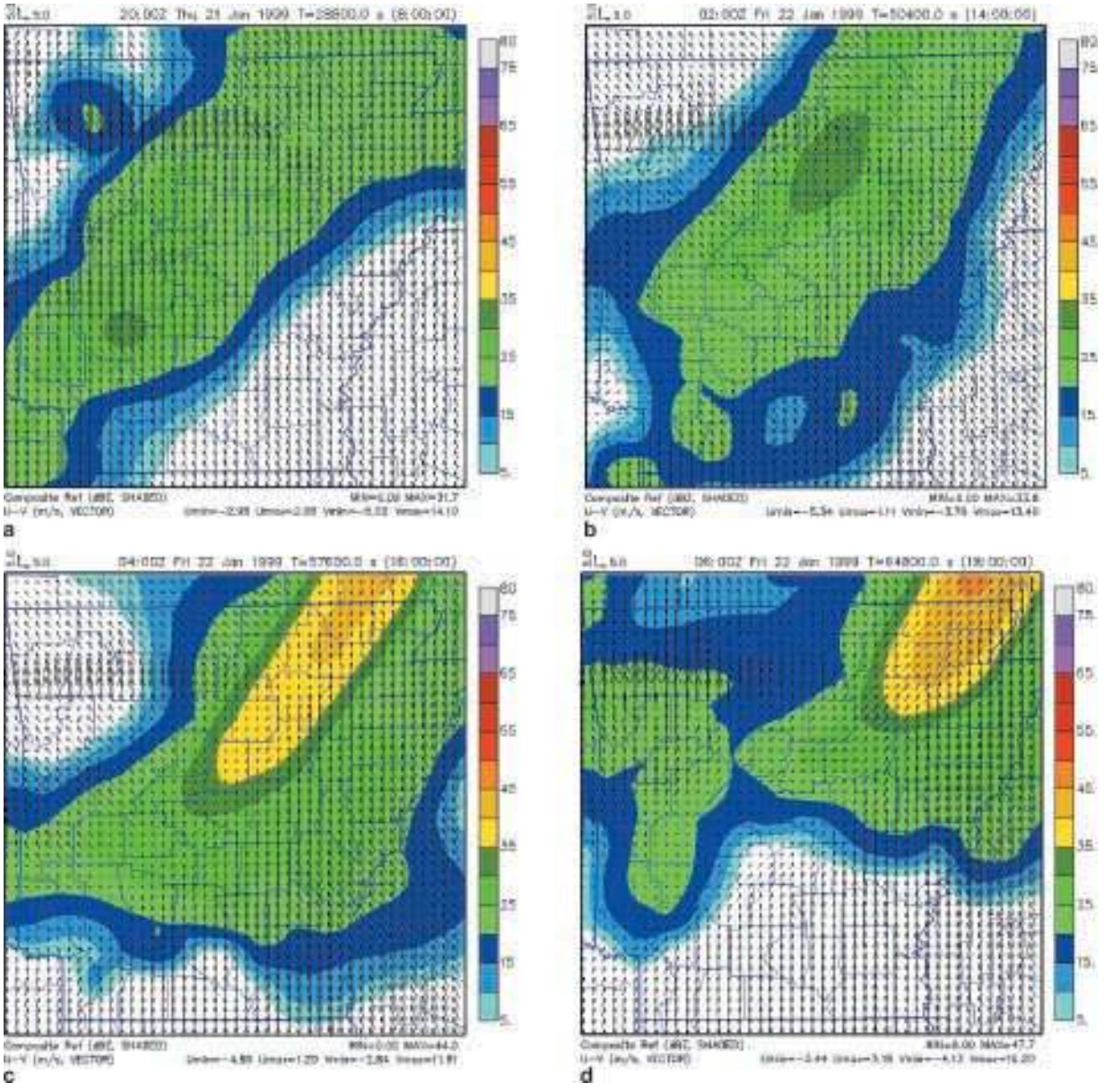

Fig. 5. Similar to Fig. 4, except for fields from the 32-km grid and at fewer times. Again the fields are interpolated to the 2-km grid before plotting

state border. Concerning this behavior, the model prediction shows an excellent agreement with the observations. The model storms did exhibit somewhat stronger rotational characteristics than the radar observation at this time, however.

Two distinct features that formed in the radar observations around this time were not reproduced by model. One is the cluster of northeastward propagating storms in the SE region of the state, some which appeared as early as 02 UTC (Fig. 3k). The other is the group of storms to the northwest of the primary line that appeared to have originated from a surface convergence boundary as early as 00 UTC (Fig. 3i). Initially, these storms were more isolated (Fig. 3k). In the region where these storms

Fig. 4. ARPS predicted reflectivity fields from the 6-km grid, at 20 UTC January 21 through 06 UTC January 22, 1999, at 2-hour intervals. To keep the presentation uniform, the 6-km fields were interpolated to the 2-km grid before being plotted for the same area

formed, a SW–NE oriented convergence line was also evident in the model surface wind fields (Fig. 3l, 3n and 3p), it, however, failed to trigger any storm along the boundary. Further to the west, the model did produce a region of light precipitation that eventually moved into the plotted domain (Fig. 3p and 3r). Proceeding this area of precipitation in Fig. 3r is a clear outflow boundary (seen in the wind field) that resembles the leading edge of radar echoes in Fig. 3q.

At 06 UTC January 22, the end time for the 2-km model run, the primary line of convection was moving out of the eastern boundary near the NE corner. The forward surge in the central portion of the line is evident in both model and observation, and the stronger cold pool behind the line in this portion must have been responsible for this behavior. The tail of this line was still trailing toward the SW. An interesting feature that developed in the model on the SE side of the tail of line is a cluster of scattered thunderstorm. Despite its noisy look, the feature turned out to be robust as sensitivity experiments with varied numerical diffusion did not change the behavior. Although these storms did not originate from exactly the right location, they do reflect the characteristics of flow in this region that were presumably responsible for triggering storms there. More detailed analyses of the data would be necessary to identify such characteristics. Another interesting feature observed in the model is the generally SW–NE oriented closely-spaced line pattern at the low levels proceeding storm initiation at both the initial and later periods, the structure was most clear in the low-level vertical vorticity fields (not shown). These may have been produced by the strong vertical shear in the region, but a complete understanding of their source and effects is not pursued here.

3.4. Discussion of results

In summary, we have presented a detailed comparison of the observed tornadic thunderstorms that occurred during the late afternoon and evening hours (local time) of January 21, 1999 in the state of Arkansas with the 2-km resolution prediction of the ARPS model. For a 10 hour period starting from 8 hours into the model run, a generally good agreement is found with respect to the number of storms in the state of AR, the rotational characteristics of storms, the speed and direction of cell movement, the organization of initially isolated cells into lines and their subsequent propagation, the transition from a straight line into a mesoscale bow-shaped echo pattern, the reasonable timing of thunderstorm initiation and cessation of new cell development, and finally, the formation of a cluster of scattered storms in the SE region of the state.

The model forecast also has some imperfections. These include the delay of initial storm initiation in the southwestern region of the state by about 2 hours, the failure to predict storms outside the primary diagonal line, position errors of up to a couple of counties (the average size of these counties is about 20 km border to border) and the general lack of anvils west of the storm cells. However, considering that the presented results are true forecasts (apart from possible assimilated observational information coming in from the 32-km grid through the much bigger 6-km grid boundaries) of 8 to 18 hours and no information was available from special observational platforms such as radar at the initial time, the agreement of the model prediction with the observation in as many details as discussed above is remarkable. Such information should no doubt provide very valuable guidance to forecasters if available in real time and many hours in advance. The results, though still limited in terms of the number of cases examined, do suggest significant predictability of convective storms, at least of this type that formed in a favorable mesoscale and large-scale environment. The predictability does depend on numerical models' ability to accurately predict the storm environment, including the surface temperature and humidity conditions, PBL mixing, and the details of the low- and upper-level flow patterns. These conditions, in turn, determine important parameters such as CAPE, CIN, vertical wind shear and low-level forcing that affect storm initiation and rotational characteristics.

Next we review how the 6-km and 32-km grids performed compared to the 2-km grid and examine the value added by the higher resolution forecast. The same fields interpolated to the 2-km grid are shown in Figs. 4 and 5 for the 6- and 32-km grids, respectively.

At 20 UTC, 8 hours into the model run, the 6-km reflectivity pattern (Fig. 4a) is very similar

to that of 2-km grid (Fig. 3b). Significant differences start to show up when storms started to form about half an hour later in the model (c.f. Fig. 3d). The 6-km run produced convection that was also biased to the north (Fig. 4b), as did the 2-km run (Fig. 3f). The tail of the 6-km convective line is somewhat better positioned, however, but it missed the activity to the SW. (The slightly poorer positioning of the 2-km forecast is believed to be due to the effect of close upstream boundary on the west side since an earlier larger 720×720 km domain run produced better positioning of the cells at this time. That run is not presented here because of a minor problem with a message-passing routine in the version of code used). In the 2 hours leading to 00 UTC (Fig. 4c), convection seen in the 6-km grid at 22 UTC has essentially died out and no new cells formed as on the 2-km grid. Isolated cells did form later between 00 and 02 UTC (Fig. 4d), in approximately the right locations (c.f. Fig. 3k). The cells are fewer in number and larger in size than the observed ones. While indications of rotation can still be seen from the wind fields and echo pattern, they are by no means as pronounced as those of 2-km forecast. These cells followed closely the observed evolution as they moved northeastward (Fig. 4e) while some new cells formed on the south side of the primary line at about 06 UTC (Fig. 4f), the latter corresponding to the cluster of cells seen in Fig. 3q. In general, the 6-km grid correctly predicted the general characteristics of the storms in the central Arkansas region in that late afternoon and evening, but with a timing delay of as much as 4 hours (the cells in Fig. 4d were not initiated until 01 UTC). This suggests that explicit grid-scale precipitation physics is still inadequate at the 6-km spatial resolution and causes a delay in the onset of convection as the weaker updraft takes longer to bring air parcels to their levels of free convection. Furthermore, it is obvious that the 2-km forecast presents much more detailed and accurate indications of the rotational characteristics of the forecast storms.

Finally, let us look at the reflectivity pattern from the 32-km grid. A broader view of the precipitation pattern on the 32-km grid was shown in Fig. 2, and the pattern was in an excellent agreement with the observations. The 32-km grid does not show the convective nature of the event until 03 UTC, when reflectivity values larger than 35 dBZ appeared (Fig. 5c, d), at about the same location as the 6-km storms (Fig. 4e, f). The 32-km grid was not capable of creating separate cells. As pointed out earlier, the 32-km reflectivity display does not include parameterized precipitation. Comparison with the total precipitation rate shows a very good agreement, the parameterization does tend to produce precipitation over a few more (32-km) grid cells on the southern edge of the reflectivity pattern. In summary, the 32-km grid played a key role in reproducing accurately the large-scale environment that fed the convective storms in this region but by itself it was incapable of providing specific, detailed guidance on the timing and location of precipitation or the type and characteristics of the systems that produced the precipitation. The 2-km forecast added undeniable value to the overall forecast.

It should be pointed the results discussed in the above are from a single set of control experiments. More insights can be gained by performing more sensitivity experiments and more detailed diagnosis of the results. Answers to such questions as the relative importance of various data sources, the necessary accuracy of the soil model initial conditions, and the performance and behavior of precipitation physics at various grid resolutions are all of great importance. In fact, a set of such sensitivity experiments has been performed and the results partially analyzed. They will be reported elsewhere.

4. Prediction of Fort Worth tornadic thunderstorms using Level-III radar data and rapid assimilation cycles

4.1. Case introduction

We present in this section another case study. At around 6:15 pm LST March 28, 2000 (00:15 UTC March 29), the downtown Fort Worth, Texas (TX) was struck by an F2 (maximum winds $51\,\mathrm{ms}^{-1}$ to $70\,\mathrm{ms}^{-1}$) tornado. The tornado developed directly over the city, descended, and stayed on the ground for at least 15 minutes. The tornado caused extensive damage to many structures, stripping glass window panes from several high-rise buildings and destroying a number of

other buildings. The tornado directly caused two deaths and many injuries. The parent storm also brought torrential rains and softball-size hail, causing two deaths from flooding in the eastern portion of the county, near Arlington, and one additional death due to hail. A second tornado from the same storm system touched down in south Arlington, some 25 kilometers east of Fort Worth, about 30 minutes later. These tornadoes have special significance because they struck the center of a major metropolitan area.

Throughout the day on March 28, a deep surface low was located over the northeastern US, and a weaker low was centered at northwestern TX (Fig. 6). A quasi-stationary front was found connecting the two low centers in between two regions of high pressure. Central and eastern TX was exposed for the entire day to southerly flow (Fig. 6). A dryline was found with a NNE–SSW orientation over western TX which progressed about 200 km eastward during the 12 hours proceeding the tornado outbreak. At 00 UTC, the dryline was located east of Abilene, about 200 km west of Fort Worth (Fig. 6b).

At upper levels at 12 UTC March 28, a ridge was found at the 500 hPa level centered over western TX and a shallow trough to the west was extending from Utah into New Mexico (NM). Central TX was located under westerly flow ahead of the ridge at this time (not shown). By late afternoon, the trough had moved eastward by about one state, with the trough line extending from Colorado into western TX near the NM border. Winds at 500 hPa level over central TX backed slightly into south–southwesterlies with significant increase in wind speed. The hodograph (not shown) from the 00 UTC Fort Worth sounding (launched from between Dallas and Fort Worth but still free of thunderstorm contamination except at the upper levels where anvils of the storms to the west were present, c.f. Fig. 7b) exhibited a clockwise rotation over a 1/8-circle arc with winds changing from 7 ms^{-1} southeasterly at the surface to 10 ms^{-1} southerly at 2.2-km level. The southerly component remained at about 10 ms^{-1} above this level while the westerly component increased to about 35 ms^{-1} at the tropopause level, resulting in an essentially straight-line hodograph above the 2.2 km level. This sounding gives rise to moderate values of low-level storm-relative helicity, suggesting potentials for moderate tornadoes.

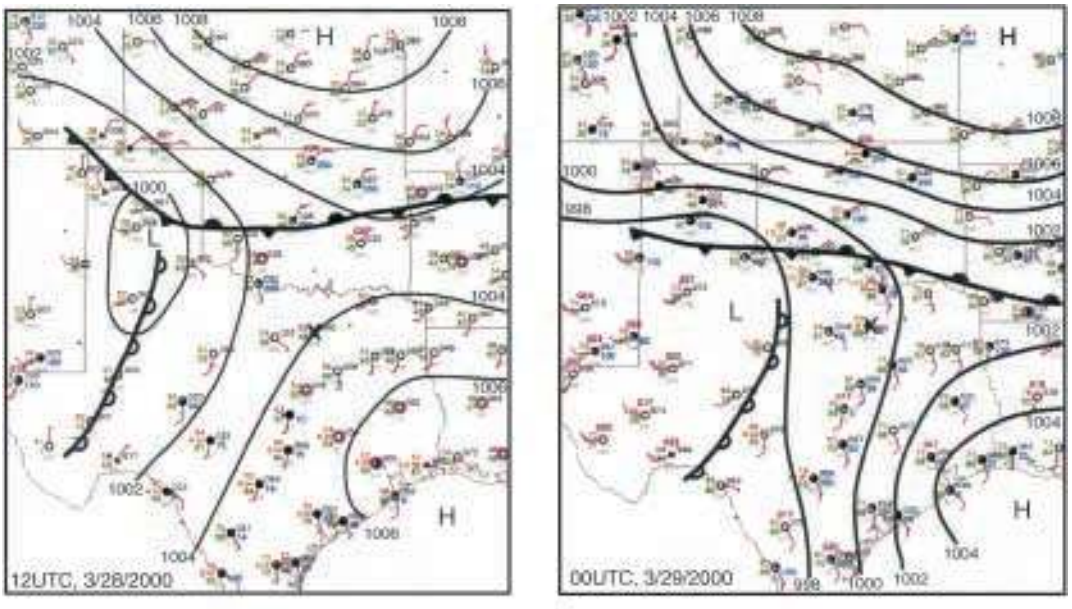

Fig. 6. Sea-level pressure and surface weather features subjectively analyzed for (**a**) 12 UTC, March 28, and (**b**) 00 UTC, March 29, 2000. A dryline is found to move from early morning (local time) position at western Texas to later afternoon location at central-western Texas. Central Texas is located in the increasingly stronger surface flow from the Gulf of Mexico. Tornado thunderstorms broke out in the later afternoon in central Texas. Fort Worth is marked by "X" in the figures

In the following, we present results from a set of prediction experiments for this case.

4.2. Design of forecast experiments

The prediction experiments were performed using the ARPS system. One of the goals of this work is to test our ability to initialize a model with pre-existing thunderstorms and deterministically predict them at fine spatial scales when using a state-of-the-art numerical model and its data assimilation system. For the latter, we are particularly interested in the impact of cloud analysis procedures in the ADAS that makes use of radar reflectivity data to initialize the water vapor, hydrometeor and temperature perturbation fields inside clouds. We also want to test the impact of assimilating these data into the model at a relatively high (~ 15 min) frequency.

For the prediction experiments, two levels of one-way nested grids were used, with the resolutions being 9 and 3 km. The two grids cover areas of 1000×1000 and $450 \times 300\,\mathrm{km}^2$, respectively. Similar to the experiments for the Arkansas tornado case, full model physics were employed, including the soil model. The Lin et al's (1983) ice microphysics scheme was used on both grids, while the Kain–Fritsch cumulus parameterization was used on the 9-km grid only. The 9-km grid was initialized at 18 UTC, March 28, from a single ADAS analysis that combined rawinsonde, wind profiler, NWS surface and Oklahoma Mesonet data and the NCEP ETA 18 UTC analysis as the background. At the lateral boundaries, the 9-km grid was forced by the ETA 18 UTC forecasts at 3-hour intervals. No radar or data assimilation was performed on the 9-km grid. The forecast was run for 12 hours, ending at 06 UTC, March 29. With the primary goal of initializing pre-existing storms, we started the 3 km grid at later times, when the thunderstorms had already formed and been observed (in precipitation mode) by the WSR-88D Doppler radars (also known as NEXRAD, Crum and Albert, 1993).

Despite recent prototyping efforts in the real-time access of WSR-88D full-volume (level-II) data (Droegemeier et al, 2002), and the ability at CAPS to ingest data from several surrounding radars in real time, (including Fort Worth) for much of the country only WSR-88D level-III (also known as NIDS, Baer, 1991) data are available in real time so far. The level-III data contains only the lowest four elevation scans and the radial velocities are quantized at about $5\,\mathrm{ms}^{-1}$ intervals. Although the latter were used in the ADAS to perform adjustments to the wind fields, they are not good enough for performing velocity and thermodynamics retrievals, however. Since the level-III data are widely available in real time, we test our ability to most effectively use them for initializing pre-existing storms in this case study.

Three forecast experiments were performed at the 3-km resolution. The first (FCST22) started from ADAS analysis at 22 UTC using the 9-km 4-hour forecast as the analysis background, the level-III reflectivity and radial velocity data from the Fort Worth, TX (KFWS), Fort Hood, TX (KGRK), Dyess Air Force Base, TX (KDYX), and Fredrick, OK (KFDR) radars, and the NWS surface observations. KGRK, KDYX and KFDR radars are located to the south–southwest, west and northwest of Fort Worth, respectively, and are about 200 km to 250 km from Fort Worth. They therefore provide a good coverage for the source regions of storms west of Fort Worth.

The second experiment (FCST23) is initialized the same way as FCST22, except at 23 UTC, one hour later. The third, which we will call the control experiment (CNTL), employed 15-min intermittent assimilation cycles that started at 22 UTC and lasted for one hour. Radar and surface data were used. The true forecast started at 23 UTC from the assimilated initial condition. Because of the non-standard initialization times, the upper level state relies heavily on information carried over from 18 UTC or even earlier (through ETA) by the coarser-resolution grid. The pre-forecast periods by the 9-km grid are generally helpful in reducing the spin-up time on the 3-km grid for both the assimilation and cold start runs (because FCST22 and FCST23 actually used 9-km forecasts as the analysis background, ''warm start'' is probably a better description for the runs).

Since the cloud analysis procedure is used, we briefly describe the package here. In order to provide detailed initial conditions for moisture variables in the ARPS, and to serve as the basis for moisture data assimilation, a cloud analysis procedure has been developed as a component of

the ADAS. The procedure is a customization of the algorithms used by the Forecast Systems Lab in the Local Analysis and Prediction System (LAPS, Albers et al, 1996) with enhancements and refinements (Zhang et al, 1998; Zhang, 1999). It incorporates cloud reports from surface stations reporting World Meteorological Organization (WMO) standard Aviation Routine Weather Reports (METARs), satellite infrared and visible imagery data, and radar reflectivity to construct three-dimensional cloud and precipitate fields. The products of the analysis package include three-dimensional cloud cover, cloud liquid and ice water mixing ratios, cloud and precipitate types, in-cloud vertical velocity, icing severity index, and rain/snow/hail mixing ratios. Cloud base, top and cloud ceiling fields are also derived. A latent heat adjustment to temperature based on added adiabatic liquid water content is applied, so that the in-cloud temperature is reasonably consistent with the water fields. More details on the package can be found in the references quoted above.

For our experiments, satellite data were not used in our cloud analyses. This is done on purpose to highlight and better evaluate the impact of level-III radar data. The simple wind adjustment procedure using radar radial velocity data is described in Brewster (1996). With the procedure, the radial winds are optimally combined with the background winds making use of their error characteristics information. It can be effective for updating the radial wind component but is not able to recover much of the tangential wind information.

4.3. Results of control experiment

Limited by space, we will present results from the 3-km grid only and we will start with control experiment CNTL. The predicted reflectivity (derived from hydrometeor fields in the same way as in Sect. 3), wind and potential temperature fields at the surface (actually at the first model level which is roughly 10 m above ground) are plotted in Fig. 8 at half hour intervals for 2.5 hours starting from 23:30 UTC, which is 1.5 hours after the data assimilation cycle is started and 0.5 hour after the true initial time at 23 UTC. All 3-km forecasts ended at 03 UTC, March 29. Figure 7 shows the corresponding low-level reflectivity fields from the level-III data of the Fort Worth radar. Tarrant and Dallas counties are highlighted in the plots with darkened borders. Downtown Fort Worth and Dallas are located roughly at the center of the left (Tarrant) and right (Dallas) counties, respectively.

At 23:30 UTC, two clusters of storms are found from both the radar observation (Fig. 7a) and in the model (Fig. 8a), one near the northwest and one at the southwest corners of the plotted domain. Each of the observed clusters contained about five reflectivity maxima, more or less related to individual storm cells. In the model, the cells are less distinct, which is believed to be due to the averaging to the relatively coarse 3-km resolution (improvements to the radar remapping methods are being pursued). The most prominent features in the surface flow are strong divergence from the storm downdrafts behind the leading gust fronts and the strong convergence at the gust front. Localized centers of maximum convergence can also be found along the gust fronts, with the strongest one located at the southeastern edge of the reflectivity maximum in the northwest cluster, close to the western border of Tarrant county. In the radar observation (Fig. 7a), a matching cell (storm A) is found located off the western border of the same county and shows radar echoes with an appendage in the southwest flank, sometimes called the hook precursor. It is this storm that spawned the Fort Worth and Arlington tornadoes, about 45 min and just over an hour later, respectively. Another more isolated cell is found about one county ($\sim$45 km) south of Tarrant county (storm B, Fig. 7a), and this cell is also reproduced well by the model (Fig. 8a).

Fig. 7. Reflectivity fields based on level-III data at approximately half an hour intervals from 23:28UTC, March 28 through 2:03UTC, March 29, 2000, from the lowest elevation (0.5°) scan of the Fort Worth radar (marked as KFWS). Also shown are county borders. Forth Worth and Dallas are located in the highlighted Tarrant (left) and Dallas (right) counties, respectively. Major storm cells are marked by capital letters. The domain shown is 200 km on each side. The two highlighted counties are about $50 \times 50\,\mathrm{km}^2$ in size

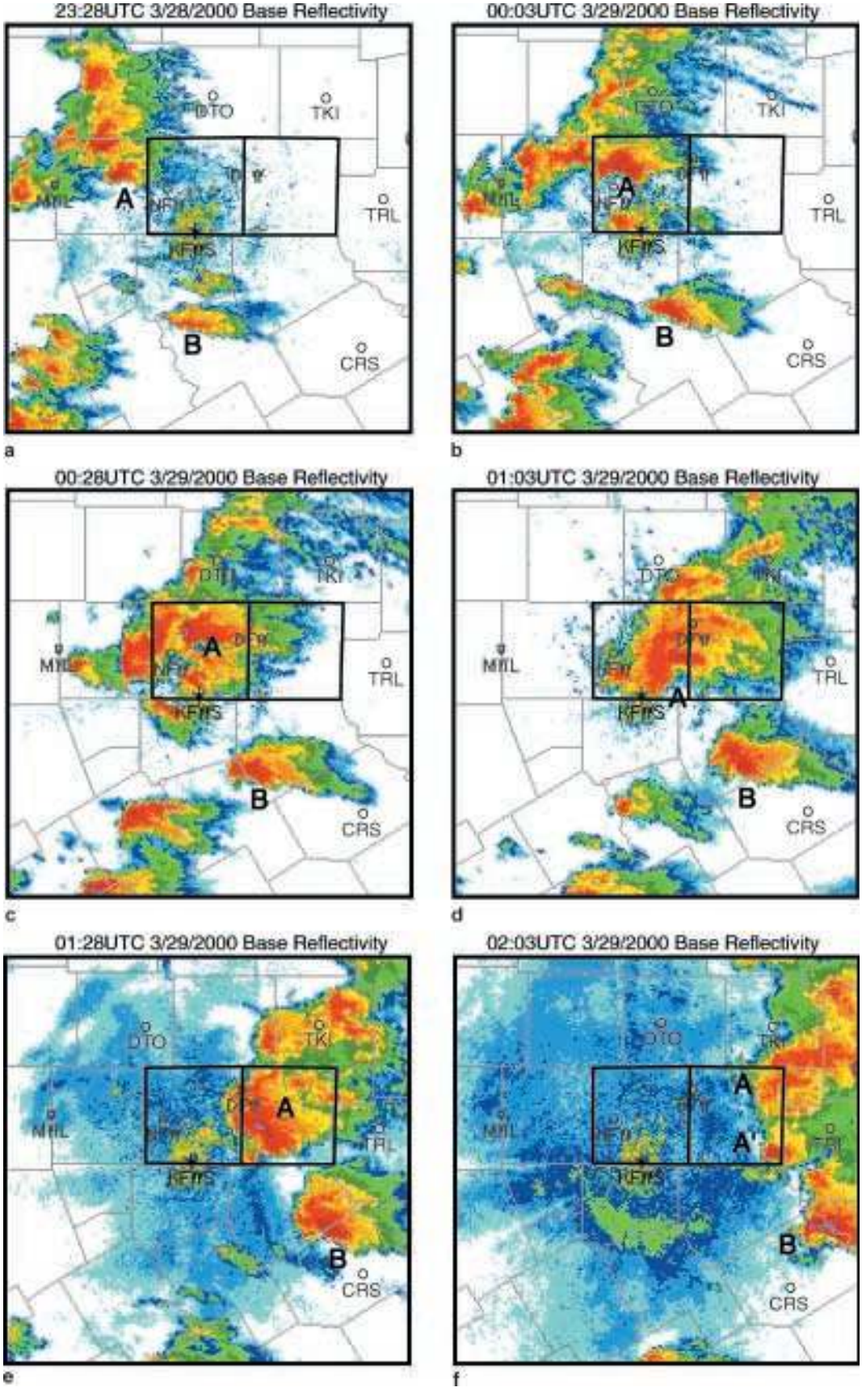
23:28UTC 3/28/2000 Base Reflectivity
00:03UTC 3/29/2000 Base Reflectivity
00:28UTC 3/29/2000 Base Reflectivity
01:03UTC 3/29/2000 Base Reflectivity
01:28UTC 3/29/2000 Base Reflectivity
02:03UTC 3/29/2000 Base Reflectivity
DTO
TKI
MHL
TRL
KFTS
CRS
A
B
a
b
c
d
e
f

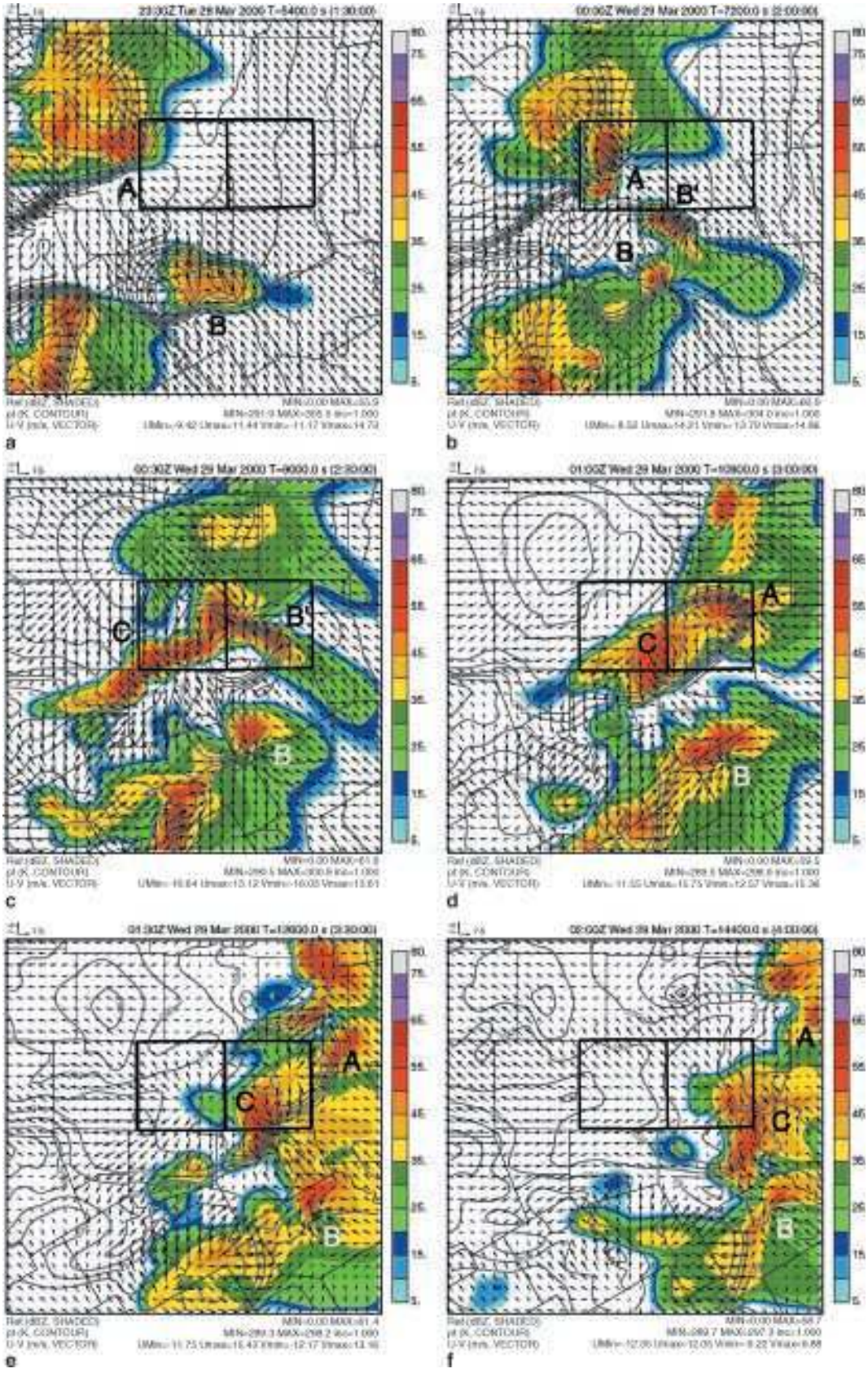

Fig. 8. Similar to Fig. 7, except that they are ground-level reflectivity fields predicted by the ARPS in the control experiment. Again major storm cells are marked by capital letters. Only the central portion of model domain is shown. The domain shown is about 200 km on each side, representing the portion of 3 km grid between 115 and 315 km in x-direction and 30 and 230 km in y-direction

Half an hour after the analysis at 00 UTC, and about 15 minutes before the Fort Worth tornado touchdown, the leading storm cell with strong low-level convergence from the northwestern cluster (storm A in Fig. 8) had moved to the western part of Tarrant county (Fig. 8b) in the model. The low-level convergence is even stronger and is located slightly west of the county center, right over downtown Fort Worth. The rear-flank-downdraft (RFD) had been significantly enhanced and the gust front associated with RFD had turned counterclockwise into a N–S orientation. It is interesting to note that a significant part of the temperature gradient seems to lag behind the leading edge of the gust front, with the latter being better defined by the surface winds. This may be an example of strong temperature gradient not being associated with the leading edge of the gust front.

By 00 UTC, the forward-flank (FF) gust front in the model had also been, as indicated by the surface temperature contours, velocity vectors as well as the reflectivity pattern, enhanced and had rotated clockwise into an E–W orientation (Fig. 8b). There existed a significant component in the surface winds that was parallel to the forward-flank gust-front. Clearly, all key ingredients found in the classical conceptual models (e.g., Lemon and Doswell, 1979) of the low-level structure of tornadic thunderstorms are in place and tornadogenesis can be expected at or near the intersecting point of the FF and RF gust fronts. Indeed, in the real world, a tornado was spawned about 15 minutes later, at a location that is almost exactly the same as suggested by the current prediction.

The forecast was not perfect, however. At the low levels, the observed radar echo is stronger on the forward flank where the rear flank echo is hardly identifiable (Fig. 7b). The echo does exhibit a hook shape on its western end at this time (Fig. 7b) and later (Fig. 7c). The composite (vertical column maximum) reflectivity plot (not shown) does show more southward extension of echo at the western end, indicating the presence of rear flank downdraft whose associated precipitation had not yet reached the ground. The precipitation in this area eventually did reach the ground, about 40 minutes later (see Fig. 7d), creating low-level echo patterns that closely match the predicted ones at and after 00 UTC.

It is seen in Fig. 8 that storm B, found at 23:28 UTC, propagated due east and developed an increasingly prominent hook shape at the western end of the echo. No information is available as to whether it produced any tornado. It is, however, one of the strongest rotating storms observed in the current domain. This storm is also reasonably well predicted by the model except for certain details. Between 23:30 and 00 UTC, the model storm split into two (denoted as B and B′ in Fig. 8), with the left member moving off to the northeast while the right mover staying its eastward course. Storm B′ eventually merged with storm A (Fig. 8b–8d) while the right member gained rotational characteristics. Throughout the time, this right mover possessed characteristics and positions (Fig. 8a–8f) that closely match the observed storm B (Fig. 7a–7f).

At 00:30 UTC, some significant differences are found between the model and observations in SW Tarrant county and further SW of that county. In the model, intense reflectivity is found extending from storm A in the NE corner of Tarrant county through the SW corner of the county and reaching the SW corner of the next county to the southwest. Such an echo is not found in the actual radar data. It was found that this line-oriented storm was triggered when the gust front from the northwestern cluster collided with the outflow on the backside of storm B. The first sign of storm initiation along the collision zone can actually be seen as early as 00 UTC in Fig. 8b. This storm moved east–northeastward and also developed significant low-level rotation later on (Fig. 8e, d). Without detailed analysis of surface flow, using, for example Doppler velocity and their retrievals, it is not clear if there was actually gust front convergence in this region and if there was, whether storm initiation was suppressed by unfavorable environmental thermodynamic conditions. One known fact is that the surface thunderstorm outflows in the model were rather strong, which was apparently helped by the cloud analysis and assimilation cycles in which hydrometeors were added into the model that in turn enhanced downdrafts and cold pools through evaporative cooling and water loading. It is possible that this part is overdone in the cloud analysis package or the analysis increments were spread over too large areas by the analysis

procedure on the still rather coarse (3-km) resolution grid.

At 00:30 UTC, despite the interferences of storms B′ and C, storm A still exhibited clear hook characteristics with a strong low-level convergence center that is located at the border of Tarrant and Dallas counties where the second tornado was reported at Arlington close to this time. The evolution of storm A in the model after 00:30 UTC differs from the observation, primary due to the interferences of storms B′ and C. Storm A in the real world moved due east after this time into Dallas county and split into two cells after it reached the eastern part of Dallas county (Fig. 7f). In the model, storm A weakened after it merged with the B′, the spuriously split member from original storm B. The combined storm moved off towards northeast. Storm C developed into a dominant cell at and after 1:30 UTC (Fig. 8e, f) that processed strong rotational characteristics that somewhat matched the real storm A.

Without a close look at the evolution history of the cells in the model, one could easily regard storm C at 2:00 UTC as storm A that is positioned half a country too far south. If, however, we take a relaxed view of cell evolution and consider storm C part of storm A (they were indeed connected from the beginning), we have a single entity that moved eastward while its southern part became dominant. By 2:00 UTC, it reached the eastern border of Dallas county with southward position error of about half a county ($\sim$25 km) compared with the radar observation. The storm cell that moved off to the northwest can be instead considered storm B′ (which is in fact quite true judging from the low-level vertical velocity fields). This view leads to a better overall agreement between the model and observation.

The above results showed that starting from an initial condition that assimilated radar and other observations over a one-hour period, the model is able to predict the timing, location and key characteristics of convective storms with very good accuracy. The correct prediction of the development of strong rotation in one of the model storms within tens of minutes and few kilometers of real tornado touchdowns is especially encouraging. Our results also show that when several storms are spaced closely, complex storm interaction can occur, through, for example, gust front collisions. Spurious cells can be triggered when such interactions are incorrectly or inaccurately handled by the model. In the following section, we will discuss the results from two other experiments that did not employ a data assimilation cycle, and through the comparisons we hope to gain additional insights on the impact of level-III radar data and of the assimilation cycle.

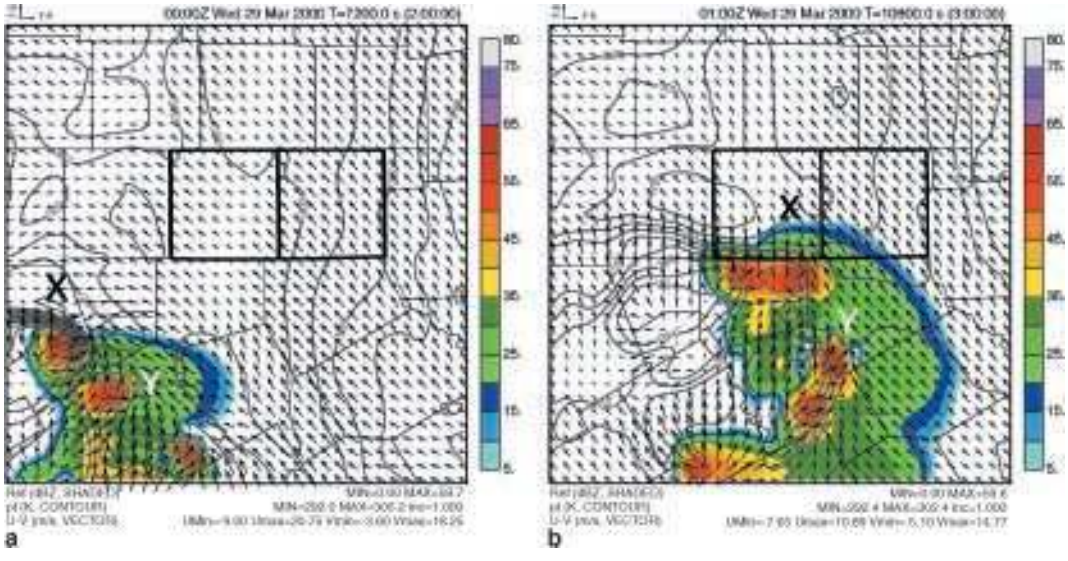

Fig. 9. Same as Fig. 8, except that they are predicted reflectivity fields from experiment FCST22 that started from initial analysis at 22 UTC, March 28, 2000. No data assimilation cycle was employed. Two model storms cells are marked as X and Y

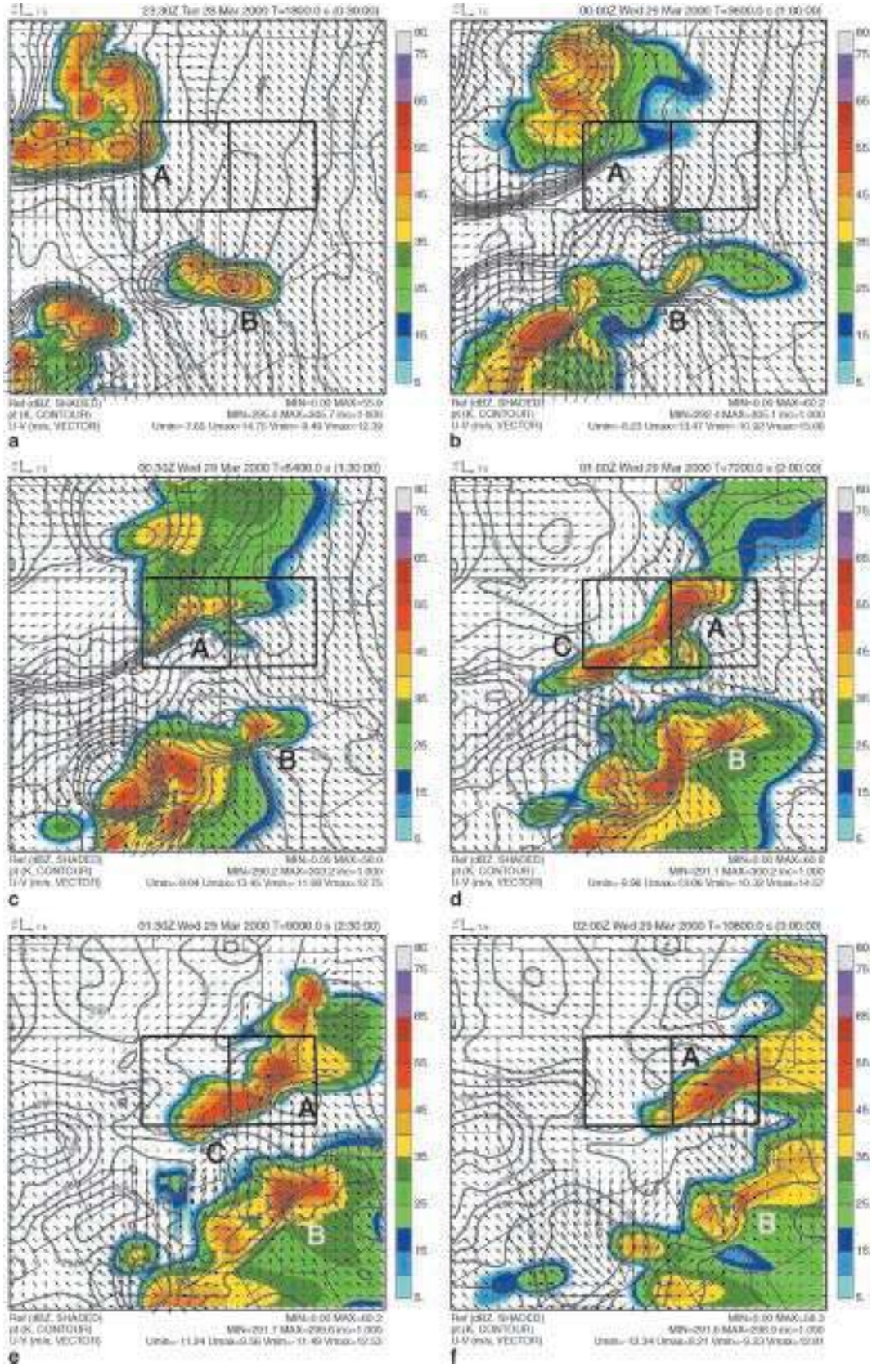

Fig. 10. Same as Fig. 9, except that they are predicted reflectivity fields from experiment FCST23 that started from initial analysis at 23 UTC, March 28, 2000. No data assimilation cycle was employed. This run had the same initial time as the control experiment shown in Fig. 8, but different initial condition

4.4. Comparison with non-cycled forecasts

The two and three-hour forecast fields from FCST22, the forecast beginning at 22 UTC and proceeding without cycled assimilation, are shown in Fig. 9. It is clear that this forecast is much worse than the control. The northwest cluster of storms is completely missing, so is storm cell B. The main predicted features in the plotted domain are three cells found at 00 UTC near the southwest corner. By 01 UTC, the two northwestern cells merged together while the one at the southern boundary split into two. They all moved in the northeast direction. There is not much correspondence between the model storms with observed ones.

The forecast fields from FCST23 corresponding to those in Fig. 7 are plotted in Fig. 10. Having been initialized one hour later than FCST22, the results are much better. All three areas of storm activity are reasonably well represented at 23:30 UTC, 30 min into the forecast. With a shorter spin-up time, the surface outflow and gust fronts are much weaker compared to CNTL. In fact, surface divergence inside the cold pool was still mostly missing at this time. In the model, storm A weakened as it propagated southeastward into Tarrant county before it intensified again after its gust front collided with the outflow from also weakening storm B (Fig. 10c and Fig. 10d). The rotational characteristics of storm A are evident but weaker than in CNTL and remained so for the rest of its life. The gust front collision also enhanced the southwestern part of storm A, and created a connected cell we call storm C. Storm B did not produce a split cell as in CNTL, but it weakened significantly and later merged with cells behind it. It is clear that the results from this run, which lacked an assimilation cycle, are not as good, and it missed the intensification of low-level convergence and rotation associated with storms A and B entirely. Such intensification is key in suggesting the high tornadogenesis potential with these storms.

4.5. Discussion

From the results of the three experiments that used level-III data in different ways, it is clear that the assimilation of the data had a significant positive impact on the forecast. The cloud analysis helped to pinpoint the location of initial storm cells and built a reasonably correct cloud structure that went on to produce the downdraft and cold pools in support of the subsequent development and evolution. The prediction of storm cells possessing strong low-level rotations at times very close to the observed times and locations of tornado touchdowns and of the low-level vortex signatures that match radar observations is especially encouraging. We plan to further analyze the data to better understand the dynamical processes involved. We also plan to apply our velocity and thermodynamic retrieval schemes to this case using full volume level-II data and further examine the impact of retrieved velocity and thermodynamic fields on the model prediction.

5. The ARPS 3DVAR system

5.1. Introduction

For the previous two case studies, the ADAS system was used for data analysis. The ADAS system is based on the Bratseth (1986) successive correction scheme. It is flexible in dealing with data of varying spatial densities and is computationally very efficient. A drawback of the Bratseth scheme, like any other non-variational scheme including the popular optimal interpolation (OI) (Bratseth scheme actually converges to OI), is that observed quantities different from the analysis variables cannot be directly analyzed. Examples of such observations include precipitable water from GPS, satellite radiances, and radar radial velocity and reflectivity. Variational methods have the advantages of being able to directly use the observations in a cost function, and through the minimization of this function, the desired analysis variables are obtained that give a best fit to the data, subjecting to background and other dynamic constraints (see, e.g., discussions in Courtier et al, 1998).

While four-dimensional variational (4DVAR) data assimilation is generally considered superior and considerable successes have been achieved in applying 4DVAR to operational systems (e.g., Rabier et al, 2000) and to small-scale applications with radar data (e.g., Sun and Crook, 2001; Gao et al, 1998), 4DVAR is computationally expensive. Furthermore, a three-dimensional variational (3DVAR) assimilation system is the

necessary first, and also computationally more efficient, step towards that the eventual goal of doing 4DVAR data assimilation. In this section, we describe the preliminary version of an incremental 3DVAR system developed recently at CAPS. An analysis example will also be given.

5.2. 3DVAR formulation

Following standard practice, we first define a cost function, J, as

$$J(\mathbf{x}) = \frac{1}{2}(\mathbf{x}-\mathbf{x}^b)^T\mathbf{B}^{-1}(\mathbf{x}-\mathbf{x}^b) + \frac{1}{2}[H(\mathbf{x})-\mathbf{y}^o]^T\mathbf{R}^{-1}[H(\mathbf{x})-\mathbf{y}^o] + J_c, \quad (1)$$

where the first term, usually called the background term, measures the departure of the analysis vector, $\mathbf{x}$, from the background, $\mathbf{x}^b$, which is weighted by the inverse of the background error covariance matrix $\mathbf{B}$. In our current scheme, the analysis vector $\mathbf{x}$ contains the three wind components (u, v, and w), potential temperature, θ, pressure, p, water vapor mixing ratio, q_v, and the mixing ratios for hydrometeor species. The second term, usually called the observation term, measures the departure of the analysis from the observation vector $\mathbf{y}^o$. The analysis is projected to the observation space by the forward operator H. For a 4DVAR implementation, H also contains the forward prediction model. The observation term is weighted by the inverse of the combined observation and observation-operator error covariance matrix $\mathbf{R}$. In an assimilation system, the background is usually a forecast valid at the analysis time. Observations that have been tested with the system include single-level surface data (including Oklahoma Mesonet), multiple-level or upper-air observations (such as rawinsondes and wind profilers), and Doppler radar radial velocity and reflectivity data.

In Eq. (1), J_c, represents dynamic constraints. For small-scale nonhydrostatic flows, this term is nontrivial because simple large-scale (e.g., geostrophic) balances are generally invalid. For analysis of radar data, especially of the radial velocity, dynamic constraints, such as the 3-D mass continuity equation and 3-D diagnostic pressure equation, are usually required. An initial version of this component, which includes mass continuity as a weak constraint and the diagnostic pressure equation as a strong constraint, has been implemented, refinement and testing of the procedure are underway. Here, we will discuss the background and observational terms only.

The 3DVAR analysis determines the model state, $\mathbf{x}$, for which J is a minimum. This occurs when the derivatives of J with respect to all control variables vanish. To avoid the computationally overwhelming problem of inverting the covariance matrix $\mathbf{B}$ in the minimization of J, and to improve the conditioning of the minimization problem, we perform, following Lorenc (1997), a transformation of control variables, from $\mathbf{x}$ to $\mathbf{v}$, according to $\sqrt{\mathbf{B}}\mathbf{v} = (\mathbf{x}-\mathbf{x}^b) = \delta\mathbf{x}$. This leads to a new representation of the cost function in incremental form:

$$J_{inc} = \frac{1}{2}\mathbf{v}^T\mathbf{v} + \frac{1}{2}(\mathbf{H}\sqrt{\mathbf{B}}\mathbf{v}-\mathbf{d})^T\mathbf{R}^{-1}(\mathbf{H}\sqrt{\mathbf{B}}\mathbf{v}-\mathbf{d}) + J_c, \quad (2)$$

where $\mathbf{H}$ is the linearized version of H and $\mathbf{d} \equiv \mathbf{y}^o - H(\mathbf{x}^b)$. With this cost function, no inversion of $\mathbf{B}$ is necessary as long as we start from a zero initial guess of $\mathbf{v}$, a common and preferred practice. Once $\mathbf{v}$ is obtained, $\mathbf{x}$ can be obtained by applying $\sqrt{\mathbf{B}}$ to $\mathbf{v}$.

To avoid explicitly storing and applying the matrix $\sqrt{\mathbf{B}}$, spatial filters have been proposed to model its effect. Gaussian-type filters were used by Daley (1991) and Huang (2001), for example. In our system, we choose the class of recursive spatial filters first proposed by Purser and McQuiqq (1982) and extended by Purser et al (2001). The filter requires no extra storage and is computationally very efficient. It asymptotically approaches the Gaussian filter when the number of applications goes to infinity. Even with only a few applications, the approximation can be rather good, especially if a high-order filter is used.

To use the filter, the matrix $\sqrt{\mathbf{B}}$ is rewritten as $\sqrt{\mathbf{B}} = \mathbf{DF}$ where $\mathbf{D}$ is a diagonal matrix consisting of the standard deviation of background errors, or, the square root of the error variances. $\mathbf{F}$ is modeled by a recursive filter, which, when using first order, is defined by

$$b_i = \alpha b_{i-1} + (1-\alpha)a_i \quad \text{for } i = 1,\ldots,n,$$
$$c_i = \alpha c_{i+1} + (1-\alpha)b_i \quad \text{for } i = n,\ldots,1, \quad (3)$$

where a_i is the initial value at grid point i, b_i is the intermediate value after a swap from $i = 1$ to n, is performed, and c_i is the final value after the filtering. α is the filter coefficient. Typically, the above algorithm is applied in all coordinate directions in succession, and the filter is applied multiple times to achieve the desired effect.

With the current implementation and the choice of primitive model variables u, v, w, θ, p, q_v and the hydrometeor species as control variables, we are not including in the background term cross-correlations between variables. The cross-correlation can be and is, however, realized through the dynamic constraints, i.e., the J_c term, in (1), but clearly those relying on quasi-geostrophic balance are not appropriate at the nonhydrostatic scale. With several existing operational 3DVAR systems (e.g., Lorenc, 1997), the cross-correlation is partially realized by choosing streamfunction and velocity potential as the control variables. The effectiveness of this approach remains to be investigated at the small scales.

In our current system, we assume that the observation errors are independent, that is, the observation error covariance matrix, **R**, is a diagonal matrix, and the diagonal elements are specified according to the estimated errors of the observations. This assumption is not as bad as it sounds when proper steps including bias correction are taken (Purser and Derber, 2001).

5.3. Example 3DVAR analysis

As a demonstration, the case of June 8, 1995 is used to test the 3DVAR scheme. It was a major day during the 1995 Verification on Onset of Rotation in Tornadoes Experiment (VORTEX 95) as several damaging tornadoes were produced by storms in the eastern Texas Panhandle. The case has been studied by Brewster (2002b). Our analyses were performed on a $73 \times 73 \times 43$ grid with a 12 km horizontal grid spacing.

During the analysis, the change in the cost function and the norm of its gradient are monitored. It was found that the cost function plotted as a function of the number of iterations started to level off after 10 and became essentially flat after 20 iterations (not shown). The decrease in the norm of the gradient continued until 50 iterations, however. Fifty iterations were used for the results presented here.

To show that the current 3DVAR system produces reasonable analysis, we compare the results with the ADAS analysis. The ADAS analysis was obtained using four correction passes with the horizontal correlation scaling parameter fixed at 50 km for all passes to facilitate easy comparison with the 3DVAR analysis. The 50 km scale was chosen to match roughly the average station density of the surface data, standard airways observations and Oklahoma Mesonet data, the primary source of data in this case. For the 3DVAR analysis, horizontally homogeneous and isotropic filter scale that is expected to yield a similar horizontal influence range as that in ADAS was used. In Fig. 11, we show the contours of east-west velocity and wind vectors at the surface and in Fig. 12 the surface potential temperature and wind vectors. Observations at the surface stations are overlaid. Comparing the 3DVAR with the ADAS and with the observations, we can see that the two analyses are comparable in quality and due to the relatively small influence range or filter scale, the analyses have a tight fit with the observations and at the same time show localized analysis increments surrounding isolated observations. In the ADAS, the inhomogeneous station density is handled by using different influence ranges for different observational networks in the multiple analysis passes, and with 3DVAR, this effect can be achieved by either using spatially inhomogeneous filter scales and/or a similar multi-pass strategy. We note that it is not our purpose here to show that one is superior to the other when we compare the 3DVAR analysis to that of ADAS. In fact, with the Bratseth scheme being able to converge to an OI scheme (Bratseth, 1986; see also Daley, 1991) which in turn can be made equivalent to a 3DVAR when only conventional data are involved (see, e.g., Courtier, 1997), it is possible to configure the 3DVAR to produce very similar results as the ADAS for this demonstration. The full advantages of 3DVAR schemes will not be realized until indirect observations are involved and when proper estimates of the background and observational error correlations are used.

Standard single-observation experiments have also been performed which confirmed that the recursive filter produces the desired spread of the observational increments. The strength of its effect depends on the number of filter passes

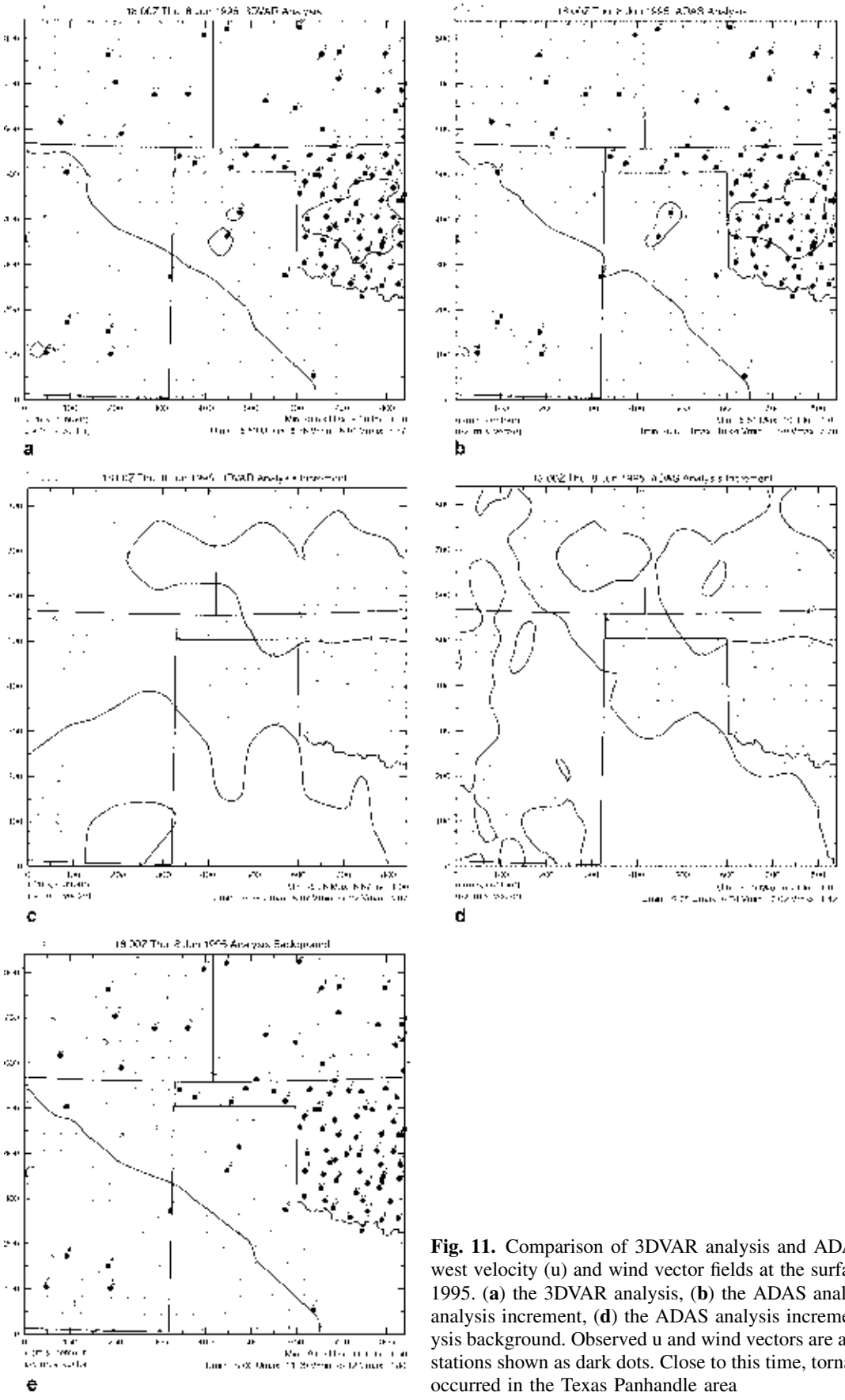

Fig. 11. Comparison of 3DVAR analysis and ADAS analysis of east–west velocity (u) and wind vector fields at the surface, for 18 Z, June 8, 1995. (**a**) the 3DVAR analysis, (**b**) the ADAS analysis, (**c**) the 3DVAR analysis increment, (**d**) the ADAS analysis increment, and (**e**) the analysis background. Observed u and wind vectors are also plotted at surface stations shown as dark dots. Close to this time, tornadic supercell storms occurred in the Texas Panhandle area

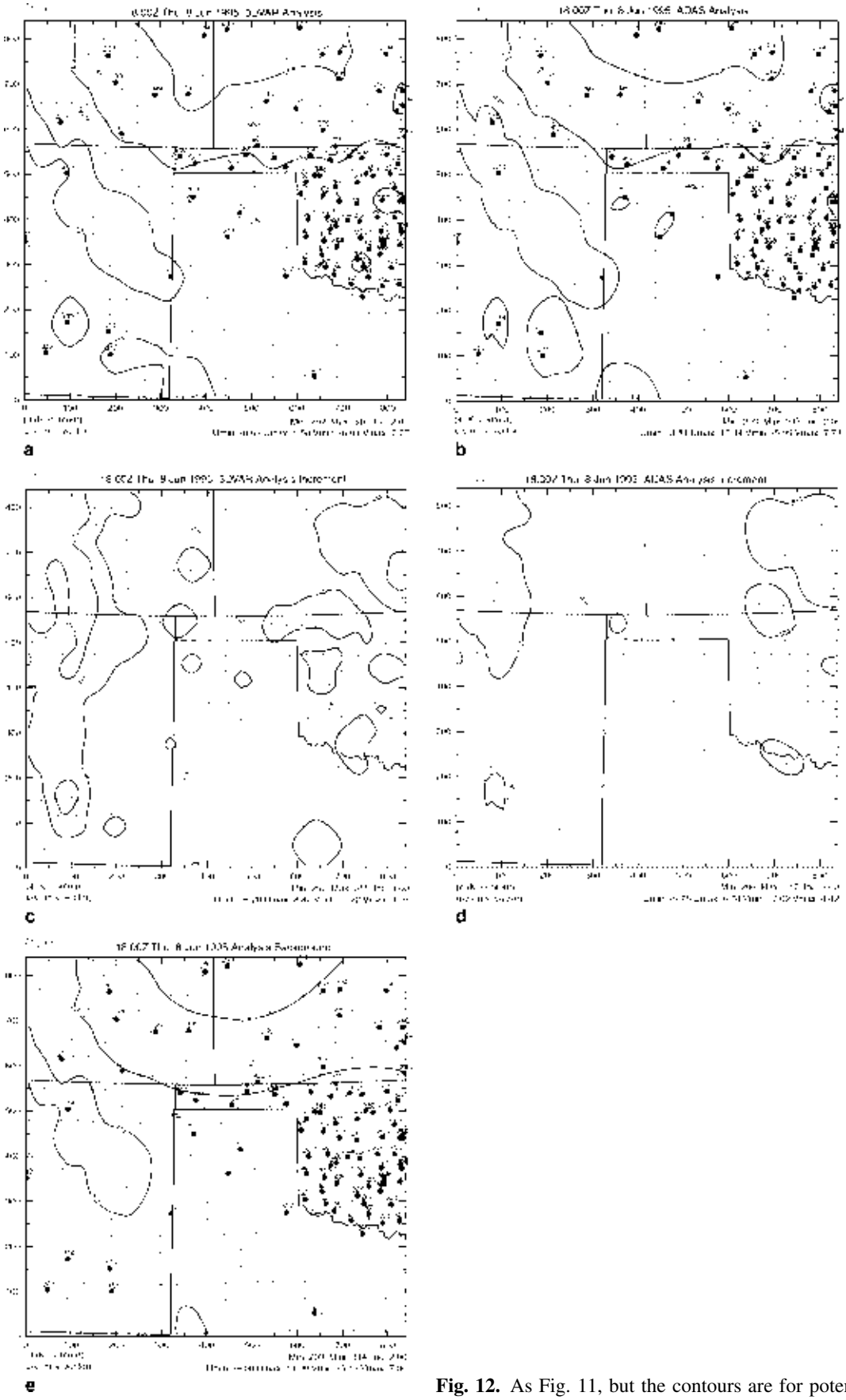

Fig. 12. As Fig. 11, but the contours are for potential temperature

used and on the correlation scale chosen. It is verified that the isotropic spread of the observation information when using a single pass of the filter agrees with theoretical estimate. As with all variational data assimilation system, careful tuning and refinement are still needed, and the true test of the analysis quality will be the quality of forecast resulting from the analysis.

Considering that weather features at the non-hydrostatic scales are often highly intermittent in both space and time and such flows tend to have much shorter lifetimes than those for which traditional 3DVAR techniques were designed for, much work is still needed in determining flow dependent, three-dimensional and anisotropic background error correlations and the filter scales, and in applying dynamics constraints suitable for flows at such scales. These are topics for continued research.

6. Summary

In this paper, we first described the current status of the Advanced Regional Prediction System of the Center for Analysis and Prediction of Storms at the University of Oklahoma. A brief outline of future plans was also given. Two rather successful cases of explicit prediction of tornadic thunderstorms were then shown. In the first case, a series of supercell storms that produced a historical number of tornadoes was successfully predicted more than 8 hours in advance. The storms agreed with observed storms to within tens of kilometers in space with initiation timing errors of less than 2 hours. The general behavior and evolution of predicted thunderstorms agreed very well with radar observations. In the second case, radar reflectivity and radial velocity were assimilated into the model at 15-minute intervals and the ensuing forecast for several hours accurately reproduced the intensification and evolution of an actual tornadic supercell that spawned two tornadoes over a major metropolitan area. These results make us optimistic about being able to deterministically predict severe convective events as such with significant lead time. To complete the paper, we briefly described a recently developed 3DVAR system in the ARPS framework. Our goal is to combine several steps of Doppler radar retrieval with the analysis of other data types into a single variational framework and eventually include the ARPS adjoint to establish a true four-dimensional variational data assimilation system. The latter developmental work will also directly contribute to the 3DVAR system of the new U.S. Weather Research and Forecast (WRF) model under development. We are especially pleased that the goals and development strategies for the WRF model are very similar to those of the ARPS about 10 years ago. This not only affirms the validity of the direction taken by CAPS, but also demonstrates the value of building upon past experience to transform research into operations.

Acknowledgment

This research was supported by NSF ATM92-20009, ATM 99-09007, NOAA NA67RJ0150 and a grant from FAA. D. H. Wang was partially supported by a research contract from Weather Decision Technology, Inc. Jason Levit is thanked for assistance handling WRS-88D tape data. Many other CAPS scientists contributed to the ARPS system testing and development. Most of the plots in the paper were generated by programs based on the ZXPLOT graphics package developed by the first author and Zuojun Zhang. Computations of the Arkansas tornado case were completed on National Center for Supercomputing Application's SGI Origin 2000 array.

References

Albers SC, McGinley JA, Birkenheuer DA, Smart JR (1996) The local analysis and prediction system (LAPS): Analysis of clouds, precipitation and temperature. Wea Forecast 11: 273–287

Baer VE (1991) The transition from the present radar dissimilation system to the NEXRAD Information Dissemination Service (NIDS). Bull Amer Meteor Soc 72: 29–33

Bischof C, Carle A, Corliss G, Griewank A, Hovland P (1992) ADIFOR – generating derivative codes from Fortran programs. Sci Progr 1: 11–29

Bratseth AM (1986) Statistical interpolation by means of successive corrections. Tellus 38A: 439–447

Brewster K (1996) Application of a Bratseth analysis scheme including Doppler radar data. Preprints, 15th Conf. Wea. Anal. Forecast. Amer. Meteor. Soc., Norfolk, VA, pp 92–95

Brewster K (1999) Phase-correction data assimilation and application to storm-scale numerical weather prediction. Ph.D. Diss., University of Oklahoma, Norman, OK

Brewster KA (2002a) Phase-correcting data assimilation and application to storm scale numerical weather prediction. Part I: Method description and simulation testing. Mon Wea Rev (accepted)

Brewster KA (2002b) Phase-correcting data assimilation and application to storm scale numerical weather prediction. Part II: Application to a severe storm outreak. Mon Wea Rev (accepted)

CAPS (1992) ARPS Version 3.0 User's Guide. Available from Center for Analysis and Prediction of Storms, University of Oklahoma, Norman OK 73019, 183 pp

Carpenter RLJ, Droegemeier KK, Bassett GM, Weygandt SS, Jahn DE, Stevenson S, Qualley W, Strasser R (1999) Storm-scale numerical weather prediction for commercial and military aviation, Part I: Results from operational tests in 1998. Preprints, 8th Conf. on Aviation, Range, and Aerospace Meteor. Amer. Meteor. Soc., Dallas, TX

Chou M-D (1990) Parameterization for the absorption of solar radiation by O_2 and CO_2 with application to climate studies. J Clim 3: 209–217

Chou M-D (1992) A solar radiation model for climate studies. J Atmos Sci 49: 762–772

Chou M-D, Suarez MJ (1994) An efficient thermal infrared radiation parameterization for use in general circulation models, NASA Tech. Memo. 104606, 85 pp. [Available from NASA Center for Aerospace Information, 800 Elkridge Landing Road, Linthicum Heights, MD 21090-2934.]

Courtier P (1997) Variational methods. J Meteor Soc Japan 75: 211–218

Courtier P, Andersson E, Keckley E, Pailleux J, Vasiljevic D, Hamurd M, Hollingsworth A, Rabier F, Fisher M (1998) The ECMWF implementation of three-dimensional variational assimilation (3D-Var). I: Formulation. Quart J Roy Meteor Soc 124: 1783–1808

Crum TD, Albert RL (1993) The WSR-88D and the WSR-88D operational support facility. Bull Amer Meteor Soc 74: 1669–1687

Daley R (1991) Atmospheric data analysis. Cambridge University Press, 457 pp

Droegemeier KK (1990) Toward a science of storm-scale prediction. Preprint, 16th Conf. on Severe Local Storms. Amer. Meteor. Soc., Kananaskis Park, Alberta, Canada

Droegemeier KK (1997) The numerical prediction of thunderstorms: Challenges, potential benefits, and results from real time operational tests. WMO Bull 46: 324–336

Droegemeier KK, Kelleher K, Crum TD, Levit JJ, Greco SAD, Miller L, Sinclair C, Benner M, Fulker DW, Edmon H (2002) Project CRAFT: A test bed for demonstrating the real time acquisition and archival of WSR-88D base (level II) data. Preprint, 18th Int. Conf. IIPS Meteor. Ocean. Hydrology. Amer. Meteor. Soc., Orlando, FL

Droegemeier KK, Xue M, Brewster K, Liu Y, Park S, Carr F, Mewes J, Zong J, Sathye A, Bassett G, Zou M, Carpenter R, McCarthy D, Andra D, Janish P, Graham R, Sanielvici S, Brown J, Loftis B, McLain K (1996) The 1996 CAPS spring operational forecasting period: Realtime storm-scale NWP, Part I: Goals and methodology. Preprints, 11th Conf. on Num. Wea. Pred. Amer. Meteor. Soc., Norfolk, VA

Droegemeier KK, Xue M, Johnson K, O'Keefe M, Sawdey A, Sabot G, Wholey S, Mills K (1995) Design and implementation of a scalable-parallel stormscale numerical weather prediction model. In: High Performance Computing (Sabot GW, ed). Reading, Mass.: Addison-Wesley, pp 45–92

Ebisuszki W, Kalnay E (1991) Ensemble experiments with a new lagged analysis forecasting scheme. 6.31–6.32, Research Activities in Atmospheric and Oceanic Modeling Rep. 15, World Meteor. Org.

Gao J, Xue M, Brewster K, Carr F, Droegemeier KK (2001a) A three-dimensional variational data assimilation scheme for storm-scale models. Preprints, 14th Conf. on Num. Wea. Pred. Amer. Meteor. Soc., Ft. Lauderdale, FL

Gao J, Xue M, Droegemeier KK, Shapiro A (2001b) A 3-D variational method for single-Doppler velocity retrieval applied to a supercell storm case. Preprints, 30th Int. Conf. Radar Meteor. Amer. Meteor. Soc., Munich, Germany

Gao J, Xue M, Shapiro A, Xu Q, Droegemeier KK (2001c) Three-dimensional simple adjoint velocity retrievals from single Doppler radar. J Atmos Ocean Tech 18: 26–38

Gao J, Xue M, Wang Z, Droegemeier KK (1998) The initial condition and explicit prediction of convection using ARPS adjoint and other retrievals methods with WSR-88D data. 12th Conf. Num. Wea. Pred. Amer. Meteor. Soc., Phoenix, AZ

Gao JD, Xue M, Shapiro A, Droegemeier KK (1999) A variational method for the analysis of three-dimensional wind fields from two Doppler radars. Mon Wea Rev 127: 2128–2142

Hou D, Kalnay E, Droegemeier KK (2001) Objective verification of the SAMEX '98 ensemble forecasts. Mon Wea Rev 129: 73–91

Huang X-Y (2001) Variational analysis using spatial filters. Mon Wea Rev 128: 2588–2600

Johnson KW, Bauer J, Riccardi GA, Droegemeier KK, Xue M (1994) Distributed processing of a regional prediction model. Mon Wea Rev 122: 2558–2572

Kain JS, Fritsch JM (1993) Convective parameterization for mesoscale models: The Kain–Fritsch scheme, The Representation of Cumulus Convection in Numerical Models, Meteor. Monogr. Amer. Meteor. Soc., pp 165–170

Kapitza H (1991) Numerical experiments with the adjoint of a non-hydrostatic mesoscale model. Mon Wea Rev 119: 2993–3011

Lafore JP, Stein J, Asencio N, Bougeault P, Ducrocq V, Duron J, Fisher C, Péreil P, Mascart P, Masson V, Pinty JP, Redelsperger JL, Richard E, Vilà-Guerau de Arellano J (1998) The meso-NH atmospheric simulation system. Part I: Adiabatic formulation and control simulation. Ann Geophys 16: 90–109

Lemon LR, Doswell CA (1979) Severe thunderstorm evolution and mesocyclone structure as related to tornadogenesis. Mon Wea Rev 107: 1184–1197

Lilly DK (1990) Numerical prediction of thunderstorms – Has its time come? Quart J Roy Meteor Soc 116: 779–798

Lin Y-L, Farley RD, Orville HD (1983) Bulk parameterization of the snow field in a cloud model. J Clim Appl Meteor 22: 1065–1092

Lorenc AC (1997) Development of an operational variational assimilation scheme. J Met Soc Japan 75: 339–346

Purser JR, Derber JC (2001) Unified treatment of measurement bias and correlation in variational analysis with consideration of the preconditioning problem. Preprints, 14th Conf. Num. Wea. Pred. Amer. Meteor. Soc., Fort Lauderdale, FL, pp 497–470

Purser RJ, Derber JC, Parrish DF, Roberts NM (2001) Numerical aspects of the application of recursive filters to variational statistical analysis with spatially inhomogeneous covariance. NOAA/NCEP Office Note 431, 34 pp

Purser RJ, McQuiqq R (1982) A successive correction analysis scheme using recursive numerical filters. Met. O 11 Tech. Note, No. 154, British Meteorological Office, 17 pp

Rabier F, Jarvinen H, Klinker E, Mahfouf J-F, Simmons A (2000) The ECMWF operational implementation of four-dimensional variational assimilation. I: Experimental results with simplified physics. Quart J Roy Met Soc 126: 1143–1170

Rogers RR, Yau MK (1989) A short course in cloud physics. Pergamon Press, Oxford, 293 pp

Schultz P (1995) An explicit cloud physics parameterization for operational numerical weather prediction. Mon Wea Rev 123: 3331–3343

Shapiro A, Droegemeier KK, Lazarus S, Weygandt S (1995a) Forward variational four-dimensional data assimilation and prediction experiments using a storm-scale numerical model. Proc., Int. Symp. on Assim. Obs. Meteor. and Oceanography. World Meteor. Org., Tokyo, Japan, pp 361–366

Shapiro A, Ellis S, Shaw J (1995b) Single-Doppler radar retrievals with Phoenix II data: Clear air and microburst wind retrievals in the planetary boundary layer. J Atmos Sci 52: 1265–1287

Shapiro A, Robinson P, Levert C, Gao J (1999) Single-Doppler velocity retrieval experiments with a simple 4DVAR technique. Preprints, 29th Int. Conf. Radar Meteor. Amer. Metero. Soc., Montreal, PQ, Canada, pp 26–29

Shapiro A, Zhao L, Zhang J, Tuttle J, Laroche S, Zawadzki I, Xu Q, Gao J (1996) Single-Doppler velocity retrievals with hailstorm data from the North Dakota thunderstorm project. Preprints, Severe Storm Conf. Amer. Meteor. Soc., San Francisco, CA, pp 546–550

Shin K-S, Chung S-K, Lee S-Y, Yoo H-D, Lee D-I, Xue M, Brewster K, Bassett G, Park S-K, Droegemeier KK (1998) Explicit realtime operational prediction of deep convection over Korea. Preprints, 16th Conf. on Wea. Anal. Forecasting. Amer. Meteor. Soc., Phoenix, AZ, pp 135–137

Skamarock WC, Klemp JB (1993) Adaptive grid refinement for two-dimensional and three-dimensional nonhydrostatic atmospheric flow. Mon Wea Rev 121: 788–804

Sun J, Crook NA (2001) Real-time low-level wind and temperature analysis using single WSR-88D data. Wea Forecast 16: 117–132

Sun J, Flicker DW, Lilly DK (1991) Recovery of three-dimensional wind and temperature fields from simulated single-Doppler radar data. J Atmos Sci 48: 876–890

Talagrand O (1991) The use of adjoint equations in numerical modeling of atmospheric circulation. Automatic differentiation of algorithms: Theory, implementation, and application. Prec. of the first SIAM workshop on automatic differentiation, Brechenridge, CO, pp 169–180

Tao W-K, Simpson J, McCumber M (1989) An ice-water saturation adjustment. Mon Wea Rev 117: 231–235

Wang Z, Droegemeier KK, White L, Navon IM (1997) Application of a New Adjoint Newton Algorithm to the 3D ARPS Storm-Scale Model Using Simulated Data. Mon Wea Rev 125: 2460–2478

Wang Z, Droegemeier KK, Xue M, Park SK (1995) Sensitivity analysis of a 3-D compressible storm-scale model to input parameters. Proc., Int. Symp. on Assim. Obs. Meteor. Oceanography. World Meteor. Org., Tokyo, Japan, pp 437–442

Weygandt S, Shapiro A, Droegemeier K (1998) The use of wind and thermodynamic retrievals to create initial forecast fields from single-Doppler observations of a supercell thunderstorm. Preprints, 11th Conf. on Wea. Anal. and For. Amer. Meteor. Soc., Phoenix, AZ, pp 286–288

Xue M (2000) High-order monotonic numerical diffusion and smoothing. Mon Wea Rev 128: 2853–2864

Xue M, Brewster K, Droegemeier KK, Wong V, Wang DH, Carr F, Shapiro A, Zhao LM, Weygandt S, Andra D, Janish P (1996a) The 1996 CAPS spring operational forecasting period: Realtime storm-scale NWP, Part II: Operational summary and examples. Preprint, 11th Conf. on Num. Wea. Pred. Amer. Meteor. Soc., Norfolk, VA, pp 297–300

Xue M, Droegemeier KK, Wong V (2000) The Advanced Regional Prediction System (ARPS) – A multiscale nonhydrostatic atmospheric simulation and prediction tool. Part I: Model dynamics and verification. Meteor Atmos Physics 75: 161–193

Xue M, Droegemeier KK, Wong V, Shapiro A, Brewster K (1995) ARPS Version 4.0 User's Guide. [Available from Center for Analysis and Prediction of Storms, University of Oklahoma, 100 E. Boyd St., Norman OK 73019], 380 pp

Xue M, Droegemeier KK, Wong V, Shapiro A, Brewster K, Carr F, Weber D, Liu Y, Wang D-H (2001) The Advanced Regional Prediction System (ARPS) – A multiscale nonhydrostatic atmospheric simulation and prediction tool. Part II: Model physics and applications. Meteor Atmos Physics 76: 143–165

Xue M, Droegemeier KK, Woodward PR (1993) Simulation of tornado vortices within a supercell storm using adaptive grid refinement technique. Preprints, 17th Conf. on Severe Local Storms, St. Louis, MO. Amer. Meteor. Soc., pp 362–365

Xue M, Hou D-C, Wang D-H, Droegemeier KK (1998) Analysis and prediction of convective initiation along a dryline. 16th Conf. Wea. Anal. Forecasting. Amer. Meteor. Soc., Phoenix, AZ, pp 161–163

Xue M, Lin S-J (2001) Numerical equivalence of advection in flux and advective forms and quadratically conservative high-order advection schemes. Mon Wea Rev 129: 561–565

Xue M, Zong J, Droegemeier KK (1996b) Parameterization of PBL turbulence in a multi-scale non-hydrostatic model. Preprint, 11th AMS Conf. Num. Wea. Pred. Amer. Metero. Soc., Norfolk, VA, pp 363–365

Zalesak ST (1979) Fully multidimensional flux-corrected transport algorithms for fluids. J Comput Phys 31: 335–362

Zhang J (1999) Moisture and Diabatic Initialization Based on Radar and Satellite Observation. PhD Thesis, University of Oklahoma, [Available from School of Meteorology, University of Oklahoma, Norman OK 73019], 194 pp

Zhang J, Carr F (1998) Moisture and latent heating rate retrieval from radar data. Preprints, 12th Conf. on Numerical Weather Prediction. Amer. Meteor. Soc., Phoenix, AZ, pp 205–208

Zhang J, Carr F, Brewster K (1998) ADAS cloud analysis. Preprints, 12th Conf. on Num. Wea. Pred. Amer. Met. Soc., Phoenix, AZ, pp 185–188

Corresponding author's address: Dr. Ming Xue, School of Meteorology, University of Oklahoma, 100 East Boyd, Norman, OK 73019, USA (E-mail: mxue@ou.edu)